

Copyright

by

Francis Alexander Norman, IV

2013

**The Thesis Committee for Francis Alexander Norman, IV
Certifies that this is the approved version of the following thesis:**

**An experimental assessment of the influence of bedforms on coupled
hyporheic flow and heat transport**

**APPROVED BY
SUPERVISING COMMITTEE:**

Supervisor:

M. Bayani Cardenas

John M. Sharp

David Mohrig

**An experimental assessment of the influence of bedforms on coupled
hyporheic flow and heat transport**

by

Francis Alexander Norman, IV, B.S.

Thesis

Presented to the Faculty of the Graduate School of

The University of Texas at Austin

in Partial Fulfillment

of the Requirements

for the Degree of

Masters of Science in Geological Sciences

The University of Texas at Austin

May 2013

Acknowledgements

This project would not have been possible without the support of many people within the UT community. First and foremost, I would like to thank my advisor, Dr. Bayani Cardenas, for his support and guidance throughout my research. I would also like to extend my gratitude to the many others who helped make my research a success:

To my committee members, Dr. Jack Sharp and Dr. David Mohrig, for reading and providing advice on my thesis.

To Dr. Audrey Sawyer, whose previous research provided a background for me to build upon, and whose assistance was invaluable in learning how to operate the laboratory flume.

To Dr. Jim Buttles, Rich Franks, and Steve McCracken, for their assistance in fixing many of the equipment malfunctions that developed over the course of my research.

To John Nowinski, who provided guidance in proper use of the data loggers, thermistors, and other laboratory equipment needed for my research.

To Travis Swanson and Kevin Befus, for helping me with various software/programming issues in MATLAB, and for providing some MATLAB codes.

To Lizhi Zheng, William Chan, and Lichun Wang, for helping me with day to day research tasks, including the heavy lifting of reshaping sediment and emptying and cleaning the flume.

Finally, to the Jackson School at UT, the National Science Foundation, and BP, for supporting me financially throughout my research.

Abstract

An experimental assessment of the influence of bedforms on coupled hyporheic flow and heat transport

Francis Alexander Norman, IV, MS Geo Sci

The University of Texas at Austin, 2013

Supervisor: M. Bayani Cardenas

Hyporheic flow influences both biogeochemical cycling in streambeds as well as streambed ecology. Some biogeochemical processes may be temperature dependent; therefore, heat transport associated with hyporheic flow may be an important influence on such cycles. I separately and experimentally assessed the effects of hyporheic flow due to bed topography on thermal dynamics in the sediment using a custom, tilting flume with temperature controls. Diel temperature cycles of 6° C were imposed in the flume and propagation of temperature signals into the sediment was examined for different bed morphologies (plane bed, pool-riffle-pool, and rippled bed), channel flow rates, and sediment grain sizes. Temperature fields in the sediment were monitored using an array of embedded thermistors, and this data was used to identify zones of upwelling and downwelling within the hyporheic zone. Results suggest that bedforms do induce substantially deeper downwelling upstream and downstream of the bedforms, with

upwelling near the crest. This in turn leads to substantial advective heat transport and distinct thermal patterns in the sediment. Variation in permeability and channel flow rates further affects the magnitude of this advective transport. These results corroborate existing theoretical models of coupled hyporheic exchange and heat transport under bedforms. Hyporheic flow therefore affects thermal patchiness in sediment, which may in turn exert a control on biogeochemical reaction rates, and form thermal refugia for fauna.

Table of Contents

List of Figures	xi
1. Introduction	1
2. Methods.....	5
2.1. Flume Setup	5
2.2. Experimental Parameters	6
2.2.1. Bedforms.....	6
2.2.2. Flow Rates	7
2.2.3. Grain Sizes.....	7
2.3. Experimental Constraints and Assumptions	8
2.4. Data Collection	8
2.5. Data Analysis.....	9
2.6. Dye tracing.....	10
3. Results.....	12
3.1. Observed Temperature Patterns for Each Trial – Amplitude Ratios	12
3.1.1. Trial 1: Pool-Riffle-Pool Topography, 500L/min Flow Rate, 2.4mm Grain Size.....	12
3.1.2. Trial 2: Pool-Riffle-Pool Topography, 250L/min Flow Rate, 2.4mm Grain Size.....	13
3.1.3. Trial 3: Pool-Riffle-Pool Topography, 125L/min Flow Rate, 2.4mm Grain Size.....	14
3.1.4. Trial 4: Rippled Bed Topography, 500L/min Flow Rate, 2.4mm Grain Size.....	15
3.1.5. Trial 5: Rippled Bed Topography, 250L/min Flow Rate, 2.4mm Grain Size.....	16
3.1.6. Trial 6: Rippled Bed Topography, 125L/min Flow Rate, 2.4mm Grain Size.....	17
3.1.7. Trial 7: Plane Bed Topography, 500L/min Flow Rate, 2.4mm Grain Size.....	18
3.1.8. Trial 8: Plane Bed Topography, 250L/min Flow Rate, 2.4mm Grain Size.....	19

3.1.9. Trial 9: Plane Bed Topography, 125L/min Flow Rate, 2.4mm Grain Size.....	20
3.1.10. Trial 10: Pool-Riffle-Pool Topography, 500L/min Flow Rate, 6.4mm Grain Size	20
3.1.11. Trial 11: Pool-Riffle-Pool Topography, 250L/min Flow Rate, 6.4mm Grain Size	22
3.1.12. Trial 12: Pool-Riffle-Pool Topography, 125L/min Flow Rate, 6.4mm Grain Size	23
3.1.13. Trial 13: Rippled Bed Topography, 500L/min Flow Rate, 6.4mm Grain Size.....	24
3.1.14. Trial 14: Rippled Bed Topography, 250L/min Flow Rate, 6.4mm Grain Size.....	24
3.1.15. Trial 15: Rippled Bed Topography, 125L/min Flow Rate, 6.4mm Grain Size.....	25
3.1.16. Trial 16: Plane Bed Topography, 500L/min Flow Rate, 6.4mm Grain Size.....	26
3.1.17. Trial 17: Plane Bed Topography, 250L/min Flow Rate, 6.4mm Grain Size.....	26
3.1.18. Trial 18: Plane Bed Topography, 125L/min Flow Rate, 6.4mm Grain Size.....	27
3.2. Temperature Dynamics Observed From Flume Experiments	27
3.3. Dye Tracing Tests.....	29
3.3.1. Trial 1: Pool-Riffle-Pool Topography, 500L/min Flow Rate, 2.4mm Grain Size.....	29
3.3.2. Trial 2: Pool-Riffle-Pool Topography, 250L/min Flow Rate, 2.4mm Grain Size.....	30
3.3.3. Trial 3: Pool-Riffle-Pool Topography, 125L/min Flow Rate, 2.4mm Grain Size.....	31
3.3.4. Trial 4: Rippled Bed Topography, 500L/min Flow Rate, 2.4mm Grain Size.....	31
3.3.5. Trial 5: Rippled Bed Topography, 250L/min Flow Rate, 2.4mm Grain Size.....	32
3.3.6. Trial 6: Rippled Bed Topography, 125L/min Flow Rate, 2.4mm Grain Size.....	33

3.3.7. Trial 7: Plane Bed Topography, 500L/min Flow Rate, 2.4mm Grain Size.....	33
3.3.8. Trial 8: Plane Bed Topography, 250L/min Flow Rate, 2.4mm Grain Size.....	34
3.3.9. Trial 9: Plane Bed Topography, 125L/min Flow Rate, 2.4mm Grain Size.....	34
3.3.10. Trial 1: Pool-Riffle-Pool Topography, 500L/min Flow Rate, 6.4mm Grain Size	34
3.3.11. Trial 2: Pool-Riffle-Pool Topography, 250L/min Flow Rate, 6.4mm Grain Size	35
3.3.12. Trial 3: Pool-Riffle-Pool Topography, 125L/min Flow Rate, 6.4mm Grain Size	36
3.3.13. Trial 4: Rippled Bed Topography, 500L/min Flow Rate, 6.4mm Grain Size.....	36
3.3.14. Trial 5: Rippled Bed Topography, 250L/min Flow Rate, 6.4mm Grain Size.....	37
3.3.15. Trial 6: Rippled Bed Topography, 125L/min Flow Rate, 6.4mm Grain Size.....	37
3.3.16. Trial 7: Plane Bed Topography, 500L/min Flow Rate, 6.4mm Grain Size.....	38
3.3.17. Trial 8: Plane Bed Topography, 250L/min Flow Rate, 6.4mm Grain Size.....	38
3.3.18. Trial 9: Plane Bed Topography, 125L/min Flow Rate, 6.4mm Grain Size.....	38
3.4. Summary of Dye Tracing Test Results.....	39
4. Discussion.....	41
4.1. Thermal Dynamics of Bedform-Induced Hyporheic Exchange	41
4.2. Possible linkages between hyporheic zone and catchment scale processes	47
4.3. Potential biological and chemical implications of thermal heterogeneity variation due to changing bedform regimes.....	48

5. Conclusions.....	50
Appendix: Figures.....	52
References.....	98

List of Figures

Figure 1.a. Groundwater system involving the hyporheic zone	52
Figure 1.b. Temperature dependence of denitrification.....	53
Figure 1.c. Concurrent diel variation of zinc concentrations and temperature.....	54
Figure 2.1.a. Schematic diagram of laboratory flume.	55
Figure 2.1.b. Image of flume with fiberglass insulation.	56
Figure 2.2.1.a. Image of flume with pool-riffle-pool topography.	57
Figure 2.2.1.b. Image of flume with rippled bed topography	58
Figure 2.2.1.c. Image of flume with flat bed topography.	59
Figure 2.4.a. Thermistor Arrays for each bedform size	60
Figure 2.4.b. Flume with HOBO U12 data loggers	61
Figure 3.1.1. Temperature Amplitude Ratios, Trial 1: Pool-Riffle-Pool Topography, 500L/min Flow Rate, 2.4mm Grain Size	62
Figure 3.1.2. Temperature Amplitude Ratios, Trial 2: Pool-Riffle-Pool Topography, 250L/min Flow Rate, 2.4mm Grain Size	63
Figure 3.1.3. Temperature Amplitude Ratios, Trial 3: Pool-Riffle-Pool Topography, 125L/min Flow Rate, 2.4mm Grain Size	64
Figure 3.1.4. Temperature Amplitude Ratios, Trial 4: Rippled Bed Topography, 500L/min Flow Rate, 2.4mm Grain Size	65
Figure 3.1.5. Temperature Amplitude Ratios, Trial 5: Rippled Bed Topography, 250L/min Flow Rate, 2.4mm Grain Size	66
Figure 3.1.6. Temperature Amplitude Ratios, Trial 6: Rippled Bed Topography, 125L/min Flow Rate, 2.4mm Grain Size	67

Figure 3.1.7. Temperature Amplitude Ratios, Trial 7: Plane Bed Topography, 500L/min Flow Rate, 2.4mm Grain Size	68
Figure 3.1.8. Temperature Amplitude Ratios, Trial 8: Plane Bed Topography, 250L/min Flow Rate, 2.4mm Grain Size	69
Figure 3.1.9. Temperature Amplitude Ratios, Trial 9: Plane Bed Topography, 125L/min Flow Rate, 2.4mm Grain Size	70
Figure 3.1.10. Temperature Amplitude Ratios, Trial 10: Pool-Riffle-Pool Topography, 500L/min Flow Rate, 6.4mm Grain Size	71
Figure 3.1.11. Temperature Amplitude Ratios, Trial 11: Pool-Riffle-Pool Topography, 250L/min Flow Rate, 6.4mm Grain Size	72
Figure 3.1.12. Temperature Amplitude Ratios, Trial 12: Pool-Riffle-Pool Topography, 125L/min Flow Rate, 6.4mm Grain Size	73
Figure 3.1.13. Temperature Amplitude Ratios, Trial 13: Rippled Bed Topography, 500L/min Flow Rate, 6.4mm Grain Size	74
Figure 3.1.14. Temperature Amplitude Ratios, Trial 14: Rippled Bed Topography, 250L/min Flow Rate, 6.4mm Grain Size	75
Figure 3.1.15. Temperature Amplitude Ratios, Trial 15: Rippled Bed Topography, 125L/min Flow Rate, 6.4mm Grain Size	76
Figure 3.1.16. Temperature Amplitude Ratios, Trial 16: Plane Bed Topography, 500L/min Flow Rate, 6.4mm Grain Size	77
Figure 3.1.17. Temperature Amplitude Ratios, Trial 17: Plane Bed Topography, 250L/min Flow Rate, 6.4mm Grain Size	78
Figure 3.1.18. Temperature Amplitude Ratios, Trial 18: Plane Bed Topography, 125L/min Flow Rate, 6.4mm Grain Size	79

Figure 3.3.1. Dye Tracing Patterns, Trial 1: Pool-Riffle-Pool Topography, 500L/min Flow Rate, 2.4mm Grain Size.....	80
Figure 3.3.2. Dye Tracing Patterns, Trial 2: Pool-Riffle-Pool Topography, 250L/min Flow Rate, 2.4mm Grain Size.....	81
Figure 3.3.3. Dye Tracing Patterns, Trial 3: Pool-Riffle-Pool Topography, 125L/min Flow Rate, 2.4mm Grain Size.....	82
Figure 3.3.4. Dye Tracing Patterns, Trial 4: Rippled Bed Topography, 500L/min Flow Rate, 2.4mm Grain Size.....	83
Figure 3.3.5. Dye Tracing Patterns, Trial 5: Rippled Bed Topography, 250L/min Flow Rate, 2.4mm Grain Size.....	84
Figure 3.3.6. Dye Tracing Patterns, Trial 6: Rippled Bed Topography, 125L/min Flow Rate, 2.4mm Grain Size.....	85
Figure 3.3.7. Dye Tracing Patterns, Trial 7: Plane Bed Topography, 500L/min Flow Rate, 2.4mm Grain Size.....	86
Figure 3.3.8. Dye Tracing Patterns, Trial 8: Plane Bed Topography, 250L/min Flow Rate, 2.4mm Grain Size.....	87
Figure 3.3.9. Dye Tracing Patterns, Trial 9: Plane Bed Topography, 125L/min Flow Rate, 2.4mm Grain Size.....	88
Figure 3.3.10. Dye Tracing Patterns, Trial 10: Pool-Riffle-Pool Topography, 500L/min Flow Rate, 6.4mm Grain Size.....	89
Figure 3.3.11. Dye Tracing Patterns, Trial 11: Pool-Riffle-Pool Topography, 250L/min Flow Rate, 6.4mm Grain Size.....	90
Figure 3.3.12. Dye Tracing Patterns, Trial 12: Pool-Riffle-Pool Topography, 125L/min Flow Rate, 6.4mm Grain Size.....	91

Figure 3.3.13. Dye Tracing Patterns, Trial 13: Rippled Bed Topography, 500L/min Flow Rate, 6.4mm Grain Size.....	92
Figure 3.3.14. Dye Tracing Patterns, Trial 14: Rippled Bed Topography, 250L/min Flow Rate, 6.4mm Grain Size.....	93
Figure 3.3.15. Dye Tracing Patterns, Trial 15: Rippled Bed Topography, 125L/min Flow Rate, 6.4mm Grain Size.....	94
Figure 3.3.16. Dye Tracing Patterns, Trial 16: Plane Bed Topography, 500L/min Flow Rate, 6.4mm Grain Size.....	95
Figure 3.3.17. Dye Tracing Patterns, Trial 17: Plane Bed Topography, 250L/min Flow Rate, 6.4mm Grain Size.....	96
Figure 3.3.18. Dye Tracing Patterns, Trial 18: Plane Bed Topography, 125L/min Flow Rate, 6.4mm Grain Size.....	97

1. Introduction

Water temperature is a critically important factor for both ecological and chemical systems in streams. At its most basic level, water temperature affects reaction rates of chemical reactions in solution, and many aquatic organisms depend on a narrow range of temperatures in order to thrive (Stanford et al., 1996).

Stream-groundwater interactions are an important component of aquatic systems (Boulton et al., 1998). Even in a stream with a net water balance that is neither significantly gaining nor significantly losing water, there can be significant exchange with the groundwater. Very shallow groundwater flow that is associated with a stream (usually the first few centimeters to meters of the bed) is called hyporheic flow, and exchange between this water and the stream is called hyporheic exchange (Alley et al. 2002; Boulton et al., 1998). Hyporheic flow is distinguished from regional groundwater fluxes in that its flow path begins and ends at the stream bed, rather than moving permanently from stream to aquifer or vice versa. The hyporheic zone has been defined several different ways, both as a physical zone and as an ecological habitat, and the boundaries of the zone are also variably defined (Boulton et. al 1998, Brunke and Gonser 1997). For the purposes of this study, the hyporheic zone will be defined as the area immediately adjacent to a stream (Figure 1.a, Alley et al. 2002) and traversed by hyporheic flow paths, in which water has neither all the characteristics of groundwater nor all those of streamwater. Streamwater and groundwater typically have different chemical and physical characteristics, and hyporheic zone water is generally a mixture of the two (Brunke and Gonser 1997).

Hyporheic exchange has been observed to impact a number of stream and stream bed processes, from cycling of nitrogen (Stanford and Ward, 1988, Storey et al. 2004, Zarnetske et al. 2011), phosphorus (Vervier et al. 2009), and organic carbon (Findlay 1995), to temperature patterns (Swanson and Cardenas 2010, Arrigoni et al., 2008; Brunke and Gonser 1997) and other physical characteristics. The hyporheic zone has been identified as both a potential source and sink for nitrogen, dependent on stream conditions (Trimmer et al. 2012), and up to 40% of total respiration within riverine ecosystems may occur within the hyporheic zone (Battin et al. 2003).

Thermal heterogeneity within the hyporheic zone develops from variable heat flux across the stream-groundwater interface. This occurs in the course of both gaining/losing exchange as well as hyporheic exchange. Within the hyporheic zone, pore water in a downwelling zone (sinking streamwater or hyporheic water) gains characteristics of thermally variable streamwater, while in an upwelling zone (rising groundwater or hyporheic water) the characteristics of the hyporheic zone are moderated by thermally stable groundwater (Boulton et al., 1998).

Several chemical processes commonly occurring within the hyporheic zone have been observed to be strongly correlated to temperature, including denitrification (Boletrou et al. 2012, Veraart et al. 2011, Figure 1.b), and cycling of metals, such as zinc (Rudall and Jarvis 2012, Nimick et al. 2003, Figure 1.c). Diel cycling of metal on concentration occurs in metal contaminated streams and has been found to be both widespread both spatially (Nimick et al. 2003) and seasonally (Nimick et al. 2005); however, its causes

remain uncertain, with some studies suggesting photosynthetically induced pH variations as the primary factor (Bourg and Boutin 1996, Bourg et al. 2000, Morris and Meyer 2005, Jones et al. 2003) and others suggesting that temperature may be an important component (Brick and Moore 1996). The connections between diel metal cycling and other potentially temperature dependent processes and hyporheic exchange are poorly understood. An early step in improving scientific understanding of this dynamic is an analysis of hyporheic exchange and thermal patterns in a typical streambed.

Bedforms are a common feature of natural stream systems that promote hyporheic exchange (Cardenas and Wilson 2007a, Swanson and Cardenas 2010). Since riffles and bedforms induce hyporheic exchange (Swanson and Cardenas 2010), they may also control thermal heterogeneity within the hyporheic zone. In turn, this heterogeneity may create patchy thermal microenvironments that act as refuges in the hyporheic zone. Since many organisms are temperature sensitive, such refuges may be key to the survival of organisms living within the hyporheic zone, and are likely to be important to ecosystem processes within the hyporheic zone (Wondzell 2011). Recent studies have in fact found measurable differences stream chemistry and in the biodiversity of macroinvertebrate communities at opposite ends of a riffle (Davy-Bowker et al. 2006, Mermillod-Blondin et al. 2000), though these differences are not necessarily tied to thermal patchiness. Thermally stable zones within the channel are less likely, and similar studies on large-woody-debris (which also drives hyporheic exchange) have found that hyporheic exchange in that case is too small to have a significant effect on channel temperatures (Sawyer et al. 2012). Bedforms or

riffles may induce more exchange than woody debris does, so their influence on channel temperatures cannot be completely ruled out. However, for the purposes of this study this effect is assumed to be negligible.

Since bedform-induced hyporheic exchange (and associated thermal cycling), is known to have chemical and biological effects (Bardini et al. 2012, Storey et al. 2004, Franken et al. 2001), transitions between bedform regimes are likely to significantly change the local biogeochemical characteristics of the transitioning stream. These changes may be non-trivial, and stream changes due to anthropogenic changes to the catchment (such as deforestation-induced erosional sediment loading) may therefore have detrimental impacts on the stream environment that may be neglected in current assessments of stream chemistry and ecosystem health. A better understanding of thermal patterns induced by bedforms will be a critical component in assessing the impact of these secondary effects. This study will assess how various common bedform parameters affect the nature of these thermal patterns, a first step in assessing their overall impact.

In this study I assess the effect of three variables (bedform topography, flow rate, and grain size/permeability) on hyporheic exchange and thermal heterogeneity within the hyporheic zone, using controlled flume experiments. I will then discuss these effects, thermal dynamics that result from bedform-induced hyporheic exchange, and the potential physical and ecological implications that arise from changes in these variables in natural systems.

2. Methods

2.1. FLUME SETUP

Experiments were conducted in a custom built recirculating flume (See Figure 2.1.a) with temperature-control and tilting capability. Flume experiments were based on earlier studies by Sawyer et al. (2012), conducted using the same flume and sediment. The flume is capable of recirculating water at rates of up to 600L/min. Typical variation in flow rate is approximately +/- 20L from the set flow rate. Sediment cannot be recirculated, so flow rates must be set so that shear stresses are low enough that grain movement does not occur. Thus, bedforms modeled in the flume are by necessity stationary.

Total flume length is approximately 7.5 m, and total internal depth is 1.25 m. The base sediment section is 5 m long by 30 cm wide by 72 cm deep. Additional sediment can be added as bedforms. Damping devices at the upstream end of the flume minimize ripples to obtain a smooth inflow into the main compartment. Flume walls were lined with insulation to minimize conduction across the flume walls (Figure 2.1.b). The flume includes three sets of dye injection ports within the sediment section to allow dye tracing tests. Each set of dye injection ports consists of 4 columns of 23 injection ports set in a panel of the flume wall. Elevation of the ports ranges from about 30-80cm above the base of the sediment column, with spacing of roughly 2cm vertically and 10 cm horizontally.

Flume surface water temperature is controlled by a heating/cooling system attached to an additional water recirculation side loop. Water from the side loop mixes with the main

recirculating loop. For each trial, a sinusoidal surface water temperature profile (amplitude = 6° C, period = 24hr) was imposed in the flume. The temperature range was initially set at 20°C-26°C for the first 6 trials, and 22°C-28°C for the final 12 trials. The change was made to reflect the increasing ambient temperature within the laboratory during the April-July timespan over which the tests were conducted.

2.2. EXPERIMENTAL PARAMETERS

Experimental parameters include: sediment size, flow rate, and bedform type. Tests were run for 2 sediment sizes, 3 flow rates, and 3 bedform types, for a total of $2 \times 3 \times 3 = 18$ trials.

2.2.1. Bedforms

Three bedform types were examined in this study. These were A) a plane bed, B) a ripple train, and C) a pool-riffle-pool system. The plane bed consisted of a level gravel surface, set even with the tops of the walls constraining the sediment column. The total depth of the sediment column was 72cm. Other bedform topographies were superimposed above this plane-bed base. The pool-riffle-pool system consisted of a 2.0 m x 0.15 m riffle in the shape of a half sinusoidal curve, positioned between 2.0 m and 4.0 m along the flume. The ripple train consisted of nine 0.5 m x 0.075 m ripples, positioned from 0.0 m to 4.5 m along the flume. Ripple crests were located at 0.375 m from the upstream end of the ripples. Figures 2.2.1a-c show the appearance of the different bedform types within the flume.

2.2.2. Flow Rates

Three flow rates were used in the study (500 L/min, 250 L/min, and 125 L/min). For each test, the depth to the crest of the bedform was set at 10 cm, producing flow velocities at 500 L/min that were just below the threshold for movement. At this flow rate, there was no grain movement, but external disturbances to the bed resulted in bed transport or saltation. Depth of flow and flow velocities varied throughout the flume, due to variable bed heights, except in the plane bed case, where velocities remained uniform throughout. Flow velocities at the bedform crest for flow rates of 500 L/min, 250 L/min and 125 L/min were 0.28 m/s, 0.14 m/s, and 0.07 m/s respectively.

2.2.3. Grain Sizes

Sediment consisted of well-sorted quartz–feldspar gravel of subangular to subrounded angularity. The smaller gravel consisted of well-sorted quartz-feldspar granules ($d_{50} = 2.4$ mm), with an approximate porosity of 0.40. Permeability was 3.4×10^{-9} m² (hydraulic conductivity 3.3×10^{-2} ms⁻¹), based on permeameter measurements on a sample of repacked flume sediment. The larger gravel consisted of well-sorted small pebbles ($d_{50} = 6.3$ mm), with an approximate porosity of 0.41. Permeability was 3.92×10^{-8} m² (hydraulic conductivity 0.39 ms⁻¹), calculated using the d_{50} value and the Kozeny-Carman equation, assuming idealized spherical sediment.

2.3. EXPERIMENTAL CONSTRAINTS AND ASSUMPTIONS

The construction of the flume imposes several constraints on the experimental methodology of this study. Since the flume lacks the capability to recirculate sediment, I cannot impose realistic sediment loading and transport conditions, and I must treat the flume as a steady state system with no sediment input. This is an unrealistic simplification, but the approximation provides an adequate picture of the impact of these bedforms on the hyporheic zone and thermal heterogeneity. This steady state assumption precludes natural sediment loading and bedform formation. Since bedforms cannot be formed naturally in the flume, I constructed them by hand using idealized topographies. The resulting system has flow rates below those that would cause the formation of the bedforms, and these rates must be kept below the threshold for sediment motion. Fine-grained gravel, rather than more commonly occurring silts and sands, was used in order to minimize time scales such as response times. With a sandy or silty sediment, response times for hyporheic flow patterns to adjust to imposed parameter changes would have been several days or weeks. Additionally, I used homogeneous, well-sorted sediment, while in natural systems, the sediment column would likely have a heterogeneous size distribution and noticeable size-grading within bedforms.

2.4. DATA COLLECTION

A temperature sensor was installed within the flume to monitor water temperature. Vertical thermistor arrays were constructed by mounting four HOBO TMC20-HD temperature sensors with an accuracy of 0.25°C and resolution of 0.03°C on each of the 18

steel rods that formed the sensor array. These rods were then inserted along the channel centerline to depths of 10, 20, 30, and 50 cm below the sediment-water interface. Wires connecting thermistors to data loggers were affixed to the flume walls to reduce flow disturbance.

Horizontal spacing of arrays was adjusted for different bedform types to allow finer spacing under smaller bedforms. Thermistor arrays and horizontal spacing for each bedform type are shown in Figure 2.4.a. Sediment and surface water temperatures were recorded every 5 min using HOBO U12 (outdoor) data loggers (Figure 2.4.b). Each trial was monitored for a minimum of 72 hrs to allow for stabilization of temperature patterns (amplitude and phase) within the sediment. Amplitude was determined by simple maxima/minima comparisons for the final 24 hour period of each trial.

2.5. DATA ANALYSIS

Thermistor data was downloaded from the HOBO data loggers after the completion of each trial, and saved using the HOBOWare Program. The data table were then exported as MS Excel files, and then converted and imported into MATLAB for analysis. Each thermistor dataset was examined graphically for apparent equipment malfunctions (usually evident as wild, impossible, and temporary divergences from the usual sinusoidal temperature profiles), and anomalous values were replaced with interpolated data to create corrected data sets. Corrected data represented only small fraction of overall data collection and were limited to only a few of the thermistors; most data sets required no correction. Malfunctioning thermistors were changed when the flume was next drained in

order to change the bedform topography, so some malfunctions carried over into multiple trials; however, these were generally not severe, and had minimal impact in the overall data set. Total data collection over the course of the project consisted of 18 trials running for a minimum of 72 hours each at 5 minute recording intervals. Each trial employed a 72-thermistor array as well as a 73rd thermistor used for recording the stream temperature, resulting in collection of over 1.1 million independent data points over the course of the study.

Using MATLAB software, the thermistor data were analyzed to determine temperature range amplitudes for each point in the sediment column. These amplitudes were then compared to the stream temperature amplitudes to create graphs of the average amplitude ration at any given point in the sediment column. These amplitude ratios are used as indicators of persistence of the “thermal signal” of the stream at depth, and thus can be used to identify regions of downwelling and upwelling hyporheic water, as well as variations in thermal heterogeneity between trials. Time series graphs were also generated for each thermistor, resulting in a total of 1296 periodic temperature curves on 324 different graphs (one for each set of 4 thermistors on a rod, for a total of 18 per trial, multiplied by 18 trials. This data was also used to generate videos that showed temporal progression of thermal propagation into the subsurface.

2.6. DYE TRACING

Dye (food coloring) was injected at several points in the sediment column (location and number variable, based on bedform type) and photographed at regular intervals (60 s

for the smaller grain size, 20 s for the larger grain size) for 4 hours or until the dye became too diffuse to accurately assess flow paths. Each injection consisted of a single pulse of a minimum of 300 μL of black dye. Dye was injected both through the injection ports and from the surface. Although the actual injection points varied with the bedform topography, for each test a minimum of five dye injections were conducted: a shallow and a deep injection below the lower stoss face, a shallow and a deep injection below the upper stoss face, and a shallow injection below the lower lee face (though most tests had several more injection points). Dye tracing tests were used for visual corroboration of flow paths assessed in heat tracing. A dye trace was conducted for each trial, resulting in the collection of over 4000 images. Photographic imagery produced in the course of the dye trace tests was assembled into short videos for the purpose of visualizing flow paths. These videos were used to help corroborate the results gleaned from the thermistor data.

3. Results

3.1. OBSERVED TEMPERATURE PATTERNS FOR EACH TRIAL – AMPLITUDE RATIOS

I present amplitude as A^* , the ratio of the amplitude of pore water temperature to surface water temperature. $A^* = 0$ indicates a constant pore water temperature and $A^* = 1$ indicates that pore water temperature tracks the surface water temperature. I define amplitude decay as how rapidly A^* approaches 0 as depth increases. “Depth” in the descriptions indicates depth below the top of the base sediment column, ignoring additional bedforms. Depth thus equal 72 cm (the top of the sediment column) – the elevation above the bottom of the sediment column. Amplitude figures for the following trials are provided following the text as Figures 3.1.1 – 3.1.18, and correspond with sections 3.1.1-3.1.18.

3.1.1. Trial 1: Pool-Riffle-Pool Topography, 500L/min Flow Rate, 2.4mm Grain Size

Amplitude decay in this trial was generally low, except in the region directly under the lee face of the riffle. Upstream of the riffle (the upper “pool”), $A^* \approx 0.6$ at 50 cm depth, and $A^* \approx 0.8$ at 10 cm and 20 cm depth. Under the base and lower reach of the riffle stoss face, decay is lower still, with $A^* \approx 1$ as deep as 20cm, and $A^* > 0.8$ as deep as 50cm. This indicates strong, deep downwelling that carries the stream temperature signal to large depths with minimal decay. Maximum amplitude ratios (and thus maximum downwelling) at depth occur roughly between a third and halfway up the stoss face. Under the lee face of the riffle, amplitude decay is rapid near the bed, and thereafter is minimal. $A^* \approx 0.3$ for all thermistors, from 10cm to 50 cm depth. This indicates upwelling of thermally stable

“groundwater” from the base of the sediment column. Downstream of the riffle (the lower “pool”), amplitude decay is comparable to that upstream of the riffle, though somewhat lower ($A^* > 0.6$ at 50cm depth, $A^* > 0.8$ at 10 cm). This is indicative of a secondary downwelling zone (of lesser magnitude than the primary downwelling zone under the stoss face). However, a fraction of the amplitude variation observed in the thermistors closest to the end of the sediment column may be the result of horizontal heat conduction through the end wall of the sediment column, as it is adjacent to the large, deep pool of “streamwater” present at that end of the flume.

3.1.2. Trial 2: Pool-Riffle-Pool Topography, 250L/min Flow Rate, 2.4mm Grain Size

Amplitude decay in this trial was generally higher than in the 500L/min trial. Upstream of the riffle (the upper “pool”), $A^* \approx 0.2$ at 50 cm depth, and $A^* \approx 0.6$ at 10 cm depth. Under the base and lower reach of the riffle stoss face, decay is lower, but still higher than that in the 500L/min test. $A^* \approx 0.8$ at 20cm, and $A^* \approx 0.4$ at 50cm. This indicates moderate downwelling that carries the stream temperature signal to large depths with moderate decay. Maximum amplitude ratios (and thus maximum downwelling) at depth occur roughly between a third and halfway up the stoss face, as in the previous test. Under the lee face of the riffle, amplitude decay is rapid near the bed, and is thereafter minimal. $A^* \approx 0.1$ at the center of the upwelling zone for all thermistors, from 10cm to 50 cm depth. This indicates upwelling of thermally stable “groundwater” from the base of the sediment column. The upwelling plume is much wider than in the 500L/min trial, indicating that while the bedform is still driving hyporheic exchange, the thermal signals

from the stream are affecting less of the sediment column before equilibrating with ambient “groundwater” temperatures. Downstream of the riffle (the lower “pool”), amplitudes are comparable to that upstream of the riffle, though somewhat higher ($A^* \approx 0.3$ at 50cm depth, $A^* \approx 0.6$ at 10 cm). This is indicative of a secondary downwelling zone (of lesser magnitude than the primary downwelling zone under the stoss face). This downwelling is also smaller in magnitude than that in the 500L/min trials. As in the prior trial, a fraction of the amplitude variation observed in the thermistors closest to the end of the sediment column may be the result of horizontal heat conduction through the end wall of the sediment column, as it is adjacent to the large, deep pool of “streamwater” present at that end of the flume.

3.1.3. Trial 3: Pool-Riffle-Pool Topography, 125L/min Flow Rate, 2.4mm Grain Size

Amplitude decay in this trial was generally higher than in the 500L/min and 250L/min trials, and the observed downwelling and upwelling were much less. Upstream of the riffle (the upper “pool”), $A^* < 0.1$ at 50 cm depth, and $A^* \approx 0.5$ at 10 cm depth. Under the base and lower reach of the riffle stoss face, decay is lower, but still higher than that in the other pool-riffle-pool tests. $A^* \approx 0.4$ at 20cm, and $A^* \approx 0.2$ at 50cm. This indicates minor downwelling that carries the stream temperature signal to moderate depths with fairly rapid decay. Maximum amplitude ratios (and thus maximum downwelling) at depth occur roughly between a third and halfway up the stoss face, as in the previous tests. Under the lee face of the riffle, amplitude decay is rapid near the bed, and is thereafter minimal. $A^* \approx 0.1$ at the center of the upwelling zone for all thermistors, from 10cm to 50

cm depth. This indicates upwelling of thermally stable “groundwater” from the base of the sediment column. The upwelling plume is much wider than in the 500L/min and 250L/min trial, indicating that while the bedform is still driving hyporheic exchange, the thermal signals from the stream are affecting less of the sediment column before equilibrating with ambient “groundwater” temperatures. The upwelling plume is also substantially weaker, unable to moderate near surface temperatures as much as those in the prior tests. It also extends further upstream, presumably due to the weaker downwelling zone having a limited range of influence within the subsurface. While the 500L/min and 250L/min trials produced notable secondary downwelling zones downstream of the riffle, in this trial downwelling in this region was minimal, with the highest amplitude ratios occurring in the most downstream thermistor, likely due to the moderating effect of the water tank at the downstream end of the flume, as discussed earlier.

3.1.4. Trial 4: Rippled Bed Topography, 500L/min Flow Rate, 2.4mm Grain Size

The rippled bed topography displays temperature patterns similar to those observed in the pool-riffle-pool, though at a smaller scale. The upstream and downstream ripples are ignored for thermal pattern analysis, as the thermistors in the rippled bed tests are concentrated near the center of the sediment column for finer scale analysis. At a 500L/min flow rate, $A^* > 0.8$ at 20 cm depth underneath the stoss face of each ripple of the central ripples (ripples 4-6 counting from upstream to downstream), indicating relatively deep downwelling. Each of these ripples also exhibits a clear upwelling zone, with A^* between 0.6 – 0.8 at 10 cm depth below each lee face. However, these zones, while similar, are not

identical between ripples. Possible causes for this are slight variation in ripple size or height, or artifacts from the thermistor spacing relative to the ripple spacing. The overall pattern bears a strong similarity to that of the pool-riffle-pool tests. The primary difference between the two is that the downwelling and upwelling zones are compressed into the space underneath the ripple, rather than extending slightly upstream and downstream of it, as they do for the larger riffle. This is a natural result of creating a ripple train, since each ripple must have both an upwelling and downwelling zone but they can't overlap with that of the neighboring ripple. The sediment column as a whole exhibits a clear secondary flow, with stronger downwelling (higher amplitudes) upstream and stronger upwelling (lower amplitudes) downstream. This secondary, larger scale flow path is likely the default state for the sediment column, and while the riffle was sufficiently large to disrupt it, the rippled bed only affects the near surface, so the overarching flow path remains. The two flow paths can be compared to basin-scale and local scale groundwater flow paths, though at a much smaller scale.

3.1.5. Trial 5: Rippled Bed Topography, 250L/min Flow Rate, 2.4mm Grain Size

At a 250L/min flow rate, $A^* \approx 0.6-0.7$ at 20 cm depth underneath the stoss face of each ripple of the central ripples (ripples 4-6 counting from upstream to downstream), indicating moderate downwelling. Each of these ripples also exhibits a clear upwelling zone, with A^* between 0.5 – 0.6 at 10 cm depth below each lee face. This indicates weaker downwelling relative to the higher flow rate, corresponding with a similar weakening of downwelling when the flow rate was decreased in the pool-riffle-pool trials. Between

ripples, there is again some variation in the magnitude of amplitudes at depth, but general patterns remain similar. The sediment column as a whole again exhibits a clear secondary flow, with stronger downwelling (higher amplitudes) upstream and stronger upwelling (lower amplitudes) downstream, though this effect is weaker than in the 500L/min test, as expected.

3.1.6. Trial 6: Rippled Bed Topography, 125L/min Flow Rate, 2.4mm Grain Size

At a 125L/min flow rate, $A^* \approx 0.6-0.7$ at only 10 cm depth underneath the stoss face of each ripple of the central ripples (ripples 4-6 counting from upstream to downstream), indicating only minor downwelling. Each of these ripples also exhibits a clear upwelling zone, with A^* between 0.4 – 0.5 at 10 cm depth below each lee face. This indicates weaker downwelling relative to the higher flow rates, corresponding with a similar weakening of downwelling when the flow rate was decreased in the pool-riffle-pool trials. Between ripples, there is again some variation in the magnitude of amplitudes at depth, but general patterns remain similar. The sediment column as a whole again exhibits a clear secondary flow, with stronger downwelling (higher amplitudes) upstream and stronger upwelling (lower amplitudes) downstream, though this effect is nearly negligible at this flow rate.

3.1.7. Trial 7: Plane Bed Topography, 500L/min Flow Rate, 2.4mm Grain Size

The plane bed topography at 500L/min produced the most irregular and unexpected results. The plane bed topography produced a large scale downwelling zone at the upstream end and a large scale upwelling zone at the downstream end, which reflects the “basin-scale” flow discussed earlier. Ideally, other fluxes should be minimal, and most heat flux should occur as the result of conduction. However, large variation in amplitude ratios at depth is observed (A^* ranges from ≈ 0.5 to ≈ 0.8 at 20 cm depth, for example, ignoring the far upstream and downstream ends of the flume). While these fluxes were substantially less than those observed at identical flow rates in the rippled bed and pool-riffle-pool trials, they were still measurable. This suggests that there is substantial upwelling and downwelling still occurring, despite the lack of bedforms to drive hyporheic fluxes.

I propose three possible explanations for this observed anomaly: remnant temperature signals from the prior rippled bed tests, minor irregularities in the bed, and uneven sediment compaction. The first theory is unlikely, as these signals persist into subsequent tests. Even if one 72-hour long trial did not provide an adequately long time for the thermal regimes to adjust to the previous flow, the later trials should not have retained these temperature signals. Additionally, the flume was stopped partially drained in order to remove the ripples, which would have removed some of the groundwater, limiting the ability of the thermal signals from the ripples to persist into the next trial. Finally, the downwelling zones had a spacing of roughly 1m, compared to ripple spacing

of 50cm. If they were remnants of the rippled bed, they would likely be more numerous and closely spaced. Minor irregularities could drive bedform induced hyporheic flow, even if they were visually negligible. In preliminary trials, leaving an exposed rod and thermistor wires in the center of the flow path was observed to induce significant downwelling, even though their horizontal cross section was $< 1\text{cm}^2$. The bed was smoothed as much as possible, using both a laser-range finder and a level water surface for leveling, but it was not a perfectly smooth surface. It is reasonable to assume that minor pits and bumps in the bed, perhaps at the sub-centimeter scale, would be capable of driving minor, but observable, hyporheic exchange. If that is the case, then it further supports the assertion that even minor bedforms can induce hyporheic exchange. Sediment compaction is another possibility, but I am not convinced that it is a reasonable explanation, as much of the upper layers of sediment was excavated and broken up in the process of removing the ripples, which would have counteracted any sediment compaction and limited pore clogging in the upper layers of sediment.

3.1.8. Trial 8: Plane Bed Topography, 250L/min Flow Rate, 2.4mm Grain Size

At a flow rate of 250L/min, the plane bed topography produced a moderate downwelling at the upstream end and a moderate upwelling at the downstream end, which reflects the “basin-scale” flow discussed earlier. Amplitude ratios were substantially lower at depth relative to the 500L/min test, indicating lower hyporheic flux rates for this flow. Ideally, other fluxes should be minimal, and most heat flux should occur as the result of conduction. However, variation in amplitude ratios at shallow depth is again observed (A^*

ranges from ≈ 0.5 to ≈ 0.8 at 10 cm depth, for instance, ignoring the far upstream and downstream ends of the flume). While these fluxes were substantially less than those observed at identical flow rates in the rippled bed and pool-riffle-pool trials, and less than those observed in the plane bed at 500L/min, they were still measureable. This suggests that there is upwelling and downwelling still occurring, despite the lack of bedforms to drive hyporheic fluxes. This is likely a result of minor topographic variations in the bed, as explained above. These upwelling and downwelling zones were observed in the same locations as in the 500L/min plane bed trial, suggesting that they have the same source in both trials.

3.1.9. Trial 9: Plane Bed Topography, 125L/min Flow Rate, 2.4mm Grain Size

In the 125L/min trial plane bed topography produces very slight downwelling at the upstream end and equally slight upwelling at the downstream end, which reflects the “basin-scale” flow discussed earlier. Other fluxes are minimal, with most heat flux apparently occurring as the result of conduction. Variation in amplitude ratios at all depths is minimal, (A^* ranges from ≈ 0.4 to ≈ 0.5 at 10 cm depth, for example, ignoring the far upstream and downstream ends of the flume). The upwelling and downwelling observed in the prior two trials were negligible in the 125L/min trial.

3.1.10. Trial 10: Pool-Riffle-Pool Topography, 500L/min Flow Rate, 6.4mm Grain Size

Amplitude decay in this trial was generally low, except the region directly under the lee face of the riffle. Upstream of the riffle (the upper “pool”), $A^* \approx 0.7$ at 50 cm depth,

and $A^* \approx 0.8$ at 10 cm and 20 cm depth. Under the base and lower reach of the riffle stoss face, decay is lower still, with $A^* > 0.8$ as deep as 50cm. This indicates strong, deep downwelling that carries the stream temperature signal to large depths with minimal decay. The thermal patterns observed in this trial generally correspond to those observed at the same flow rate with smaller sediment, but the depth of penetration of temperature signals is generally greater. One exception to this is that the very high amplitude temperature signals ($A^* > 0.9$) do not appear to penetrate past the uppermost layers of the sediment in this trial, while with the smaller sediment $A^* \approx 1$ was observed as deep as 20 cm or more. I am not sure whether this is an artifact of my amplitude calculation method, or whether it is reflective of heat loss through the walls and base of the flume. Maximum amplitude ratios (and thus maximum downwelling) at depth occur roughly between a third and halfway up the stoss face, as was the case with the smaller sediment size. Under the lee face of the riffle, amplitude decay is more noticeable, with $A^* = 0.7 - 0.5$ in the upwelling plume. These amplitude ratios are indicative of highly variable temperature regimes when compared to similar locations in the smaller sediment trials, but they are still substantially less variable than the downwelling zones, and indicate upwelling. In this case, the thermally stable “groundwater” from the base of the sediment column is more affected by the downwelling temperature signals, and thus is less thermally stable than it otherwise would be. This decreased thermal instability is then transmitted to the upwelling water column. Downstream of the riffle (the lower “pool”), amplitude decay is comparable to that upstream of the riffle, though somewhat lower ($A^* \approx 0.7$ at 50cm depth, $A^* \approx 0.8$ at

10 cm). This is indicative of a secondary downwelling zone (of lesser magnitude than the primary downwelling zone under the stoss face). There may also be another upwelling zone, indicating the possibility of re-emergence of “basin-scale” flow, as the increased permeability becomes more dominant than the bedform-induced flow. However, this assertion is speculative as the variation is too small to make a definite conclusion.

3.1.11. Trial 11: Pool-Riffle-Pool Topography, 250L/min Flow Rate, 6.4mm Grain Size

Amplitude decay in this trial was generally more rapid than in the Trial 10, but less so than Trial 2. Upstream of the riffle (the upper “pool”), $A^* \approx 0.4$ at 50 cm depth, and $A^* \approx 0.9$ at 10 cm depth. Under the base and lower reach of the riffle stoss face, decay is lower, but still higher than that in the 500L/min test. $A^* \approx 0.8$ at 20cm, and $A^* \approx 0.6$ at 50cm. This indicates moderate to strong down downwelling that carries the stream temperature signal to large depths with moderate decay. Maximum amplitude ratios (and thus maximum downwelling) at depth occur roughly between a third and halfway up the stoss face, as in the previous tests. Under the lee face of the riffle, amplitude decay is rapid near the bed, and is thereafter minimal. $A^* \approx 0.2$ at the center of the upwelling zone for all thermistors, from 10cm to 50 cm depth. This indicates upwelling of thermally stable “groundwater” from the base of the sediment column is present in this trial. Downstream of the riffle (the lower “pool”), amplitudes are comparable to not comparable to those upstream of the riffle, contrary to the pattern with smaller sediment, which produces a secondary downwelling zone. The strong exchange appears to overwhelm the secondary downwelling zone, preventing its occurrence. As in several the prior trials, a fraction of

the amplitude variation observed in the thermistors closest to the end of the sediment column may be the result of horizontal heat conduction through the end wall of the sediment column, as it is adjacent to the large, deep pool of “streamwater” present at that end of the flume. This effect is magnified by the increased permeability, so that A^* is high at depth near the downstream end of the flume.

3.1.12. Trial 12: Pool-Riffle-Pool Topography, 125L/min Flow Rate, 6.4mm Grain Size

Amplitude decay in this trial was generally more rapid than in the Trials 10 and 11, and the observed downwelling and upwelling were much less, but greater than the corresponding Trial 3. Upstream of the riffle (the upper “pool”), $A^* \approx 0.1$ at 50 cm depth, and $A^* \approx 0.6$ at 10 cm depth. Under the base and lower reach of the riffle stoss face, decay is lower, but still higher than that in the other pool-riffle-pool tests. $A^* \approx 0.5$ at 20cm, and $A^* \approx 0.2$ at 50cm. This indicates minor downwelling that carries the stream temperature signal to moderate depths with fairly rapid decay. Maximum amplitude ratios (and thus maximum downwelling) at depth occur roughly between a third and halfway up the stoss face, as in the previous tests. Under the lee face of the riffle, amplitude decay is rapid near the bed, and is thereafter minimal. $A^* \approx 0.2-0.4$ at the center of the upwelling zone for all thermistors. Upwelling does not appear as strong as with smaller sediment, likely due to the increased permeability, which hastens heat transfer from the surface. It shares other characteristics with the upwelling zone in Trial 3, being less distinct and wider than the upwelling zones in Trials 10 and 11. Secondary downwelling was observed, though it was extremely minor, with horizontal variation of amplitude ratios of only less than 0.1. An

additional upwelling zone appears to occur further downstream, lending further support to the suggestion that “basin-scale” flow is occurring in this pool-riffle-pool system due to increased permeability.

3.1.13. Trial 13: Rippled Bed Topography, 500L/min Flow Rate, 6.4mm Grain Size

At a flow rate of 500L/min, the presence of ripples in a sediment with such high permeability results in extremely high rate of hyporheic exchange, which results in almost all of the sediment column having an amplitude ratio of $A^* > 0.8$. As a consequence, drawing meaningful inferences from this trial is difficult. As with the previous ripple tests, the upstream and downstream ripples are ignored for thermal pattern analysis, as the thermistors in the rippled bed tests are concentrated near the center of the sediment column for finer scale analysis. At a 500L/min flow rate, $A^* \approx 1$ for much of the sediment, so observing upwelling and downwelling zones is impossible for several ripples. However, some ripples do exhibit faint traces of upwelling, which suggests that the hyporheic flow is behaving appropriately, even if the temperatures are fairly homogeneous. The sediment column as a whole exhibits a clear secondary flow (though here it may be the primary flow) with slightly stronger downwelling (higher amplitudes) upstream and slightly stronger upwelling (lower amplitudes) downstream.

3.1.14. Trial 14: Rippled Bed Topography, 250L/min Flow Rate, 6.4mm Grain Size

At a 250L/min flow rate, $A^* > 0.9$ at 10 cm depth underneath the stoss face of each ripple of the central ripples (ripples 4-6 counting from upstream to downstream), indicating strong

downwelling. Each of these ripples also exhibits a clear upwelling zone, with A^* between 0.6 – 0.8 at 10 cm depth below each lee face. Between ripples, there is again some variation in the magnitude of amplitudes at depth, but general patterns remain similar. The sediment column as a whole again exhibits a clear secondary flow, with stronger downwelling (higher amplitudes) upstream and stronger upwelling (lower amplitudes) downstream, though this effect is weaker than in the 500L/min test, as expected. Magnitudes of all upwelling and downwelling are greater than those observed for smaller sediment sizes in trial 5.

3.1.15. Trial 15: Rippled Bed Topography, 125L/min Flow Rate, 6.4mm Grain Size

At a 125L/min flow rate, $A^* \approx 0.8$ at only 10 cm depth underneath the stoss face of each ripple of the central ripples (ripples 4-6 counting from upstream to downstream), indicating moderate downwelling. Each of these ripples also exhibits a clear upwelling zone, with $A^* \approx 0.6$ at 10 cm depth below each lee face. This indicates weaker downwelling relative to the higher flow rates, but stronger downwelling compared to the smaller sediment test in Trial 6. Between ripples, there is again some variation in the magnitude of amplitudes at depth, but general patterns remain similar. The sediment column as a whole again exhibits a clear secondary flow, with stronger downwelling (higher amplitudes) upstream and stronger upwelling (lower amplitudes) downstream, though this effect is weaker than in the higher flow-rate tests, as expected.

3.1.16. Trial 16: Plane Bed Topography, 500L/min Flow Rate, 6.4mm Grain Size

As with test 13, the majority of the sediment columns experienced extreme temperature variations, with $A^* \approx 1$ for most sediment. The only stable temperature zone within the measured region was at the far downstream end of the sediment column, where there was some evidence of upwelling. This result was somewhat unexpected, as the presumption is that for a plane bed, most heat transport will be conduction dominated. However, the extremely high permeability associated with the larger grain size presumably allowed the formation of a strong “basin-scale” current of groundwater that spanned the length of the flume, allowing deep penetration of temperature signals. This flow path must be rapid and must include the entire basin, since the lack of a strong upwelling zone indicates that there is not time for the “groundwater” to reach a stable temperature before being forced up and out of the sediment column. The irregularities and anomalous downwelling and upwelling noted in the plane-bed tests with the small sediment did not occur in this set of plane-bed trials.

3.1.17. Trial 17: Plane Bed Topography, 250L/min Flow Rate, 6.4mm Grain Size

At a flow rate of 250L/min, the plane bed topography produced significant downwelling at the upstream end and significant upwelling at the downstream end, which reflects the “basin-scale” flow discussed earlier. At the upstream end of the flume, $A^* \approx 0.7 - 0.8$ at 50cm depth and $A^* > 0.9$ at 10cm depth while at the downstream end of the flume, $A^* < 0.2$ at both 10cm and 50cm. Amplitude ratios were substantially lower at

depth relative to the 500L/min test, but were higher than any of the plane-bed tests with the smaller sediment size.

3.1.18. Trial 18: Plane Bed Topography, 125L/min Flow Rate, 6.4mm Grain Size

In the 125L/min trial plane bed topography produces moderate downwelling at the upstream end and moderate upwelling at the downstream end (compared to slight upwelling at the same flow rate with smaller sediment). Other fluxes are minimal, with most heat flux apparently occurring as the result of conduction. Amplitude of temperature signals decays far more rapidly than in Trial 16 or Trial 17. At the upstream end of the flume, $A^* \approx 0.3$ at 50cm depth and $A^* > 0.9$ at 10cm depth while at the downstream end of the flume, $A^* 0.3 - 0.4$ at both 10cm and 50cm.

3.2. TEMPERATURE DYNAMICS OBSERVED FROM FLUME EXPERIMENTS

Deep penetration of stream temperature signals (high temperature amplitudes at depth) indicates downwelling zones, where thermal advection is high. Shallow penetration of temperature signals (low amplitude ratios) indicates upwelling zones, where deep “groundwater” moderates temperatures. High amplitude variation and rapid decay of amplitude ratios with increasing depth, indicate neither strong upwelling nor strong downwelling (most heat/water exchange is by conduction/diffusion).

A total of 18 trials were conducted, using flow rate, grain size, and bedform regime as variables. In trials 1-3 (pool-riffle-pool), the riffle drives hyporheic exchange and thermal advection in the hyporheic zone, resulting in a characteristic hyporheic temperature

pattern. Temperature amplitude ratios at depth (relative to stream temperature) peak immediately upstream of the riffle and under its lower stoss face, with secondary local maxima observed immediately downstream of the riffle in some trials. Amplitude ratio minima occur underneath the crest and lee face of the bedform. In trials 4-6 (rippled bed), the bedforms induce similar patterns, with local amplitude maxima beneath each stoss face, and local minima beneath the lower lee face and trough of the ripple train. In trials 7-9, (plane bed trials), temperature patterns showed minimal horizontal variation, and amplitudes of temperature variation decayed rapidly with increasing depth, relative to tests with bedforms, indicating minimal advective heat exchange. Some variation was still present, likely attributable to small bedforms still remaining on the bed.

Flow rate was inversely correlated with rapidity of amplitude decay across all bedform types and grain sizes, with greater flow rates (all other factors equal) resulting in decreased amplitude decay at depth in each case. Amplitude patterns thus varied in magnitude with variations in flow rate, but otherwise remained similar in shape. Plane bed trials also adhered to this pattern, suggesting that while advective heat exchange in such systems is minimal relative to other bedform regimes, it is not insignificant (temperature exchange driven solely by conduction would not vary with flow rate).

Grain size was also inversely correlated with amplitude decay at depth, with larger grain sizes increasing temperature amplitudes at all depths for all bedform regimes and flow rates. The larger grain size (6.4mm) had sufficient permeability to allow significant advective transport for all bedform regimes, and in several cases some thermistors as deep

as 50 cm tracked the surface temperature at nearly a 1:1 ratio. Variations in amplitude patterns between sediment sizes were primarily confined to changes in magnitude (as in the case of variation in flow rate). However, the coarser sediment induced a slight change in the shape of the amplitude patterns. Amplitude patterns in the coarser sediment generally resembled those in the finer sediment, but with increased advection at the upstream end of the flume and decreased advection at the downstream end of the flume. Since the coarser sediment allows for greater advection, hyporheic flow patterns begin to come in contact with the base of the sediment column, resulting in merging of the flow patterns with the underlying “basin scale” flow path that traverses the entire sediment column of the flume. At large grain sizes, this additional flow becomes significant enough to transfer notable quantities of heat through the sediment column, creating this secondary temperature pattern.

3.3. DYE TRACING TESTS

Dye tracing tests were conducted for each trial. Figures 3.3.1 – 3.3.18 present sample imagery and flow paths for each test, corresponding to sections 3.3.1 – 3.3.18.

3.3.1. Trial 1: Pool-Riffle-Pool Topography, 500L/min Flow Rate, 2.4mm Grain Size

Dye was injected at 10 points in the sediment column upstream, downstream, and directly underneath the lower stoss and lee faces of the riffle. Dye tracing results corroborated thermal studies. Dye injected upstream of the riffle crest moved in downward

arcs, emerging at or near the riffle crest, while dye injected downstream of the riffle, or under its lee face, exhibited retrograde motion, emerging on the lee face of the riffle. Locations of downward and upward motion of dye corresponded with the locations of downwelling and upwelling zones inferred from the thermistor data. These patterns of dye movement thus reflect prevailing models of bedform-induced flow paths and support the assertion that hyporheic heat flow observed in the thermal studies is caused by this bedform-induced hyporheic exchange.

3.3.2. Trial 2: Pool-Riffle-Pool Topography, 250L/min Flow Rate, 2.4mm Grain Size

Dye was injected at 10 points in the sediment column upstream, downstream, and directly underneath the lower stoss and lee faces of the riffle. Dye tracing results corroborated thermal studies. Dye injected upstream of the riffle crest moved in downward arcs, emerging at or near the riffle crest, while dye injected downstream of the riffle, or under its lee face, exhibited retrograde motion, emerging on the lee face of the riffle. Patterns of dye motion were similar to those in the 500L/min test, but the dye moved less rapidly, especially in the secondary downwelling zone downstream of the riffle. Locations of downward and upward motion of dye corresponded with the locations of downwelling and upwelling zones inferred from the thermistor data, as in the previous trial. These patterns of dye movement thus reflect prevailing models of bedform-induced flow paths and support the assertion that hyporheic heat flow observed in the thermal studies is caused by this bedform-induced hyporheic exchange.

3.3.3. Trial 3: Pool-Riffle-Pool Topography, 125L/min Flow Rate, 2.4mm Grain Size

Dye was injected at 10 points in the sediment column upstream, downstream, and directly underneath the lower stoss and lee faces of the riffle. Dye spread rapidly downward in the first few minutes of the test. This is presumed to be the result of the dye density being slightly different than that of the groundwater (possibly due to differing initial temperatures). After a few minutes, the dye began to equilibrate with the surrounding water and downward motion began to slow. In previous trials, this motion was presumably overwhelmed by rapid advection, which limited the relative impact of downward motion and sped the process of equilibration. After the initial movement, further movement of dye consisted of very slow horizontal motion. Dispersion of dye also prevented the entire flow paths from being observed, since the time scales for flow through the subsurface were too long for the dye to pass through a full flow path without dissipating to a point where it could not be accurately tracked. These dye movement patterns (i.e., the lack of the arcing patterns from the prior trials) indicate that bedform induced advection in this case is far less than that in the 500L/min and 250L/min trials (corresponding with the smaller advection values inferred from the thermistor data), and is overwhelmed by density driven advection and dispersive effects.

3.3.4. Trial 4: Rippled Bed Topography, 500L/min Flow Rate, 2.4mm Grain Size

Dye was injected at 11 points in the sediment column at various depths beneath a ripple train. Dye injected at shallow depths under the lee face of a ripple, or under the base of the trough, exhibited retrograde motion toward the crest. Dye injected on the lower stoss

face of the ripple exhibited clear downwelling, reaching its greatest depth (~20cm) underneath the ripple crest, before rising on the lee face. Dye patterns did tend to sink rapidly in the first few minutes of the test (evidence of more density driven advection), though at some near-surface injection points this motion was overwhelmed by rapid advection. This sinking effect tended to split the dye injected at moderate depths (~10-20 cm) into two paths, with dye following both the arcing paths induced by the ripple train and sinking into a slower, larger scale flow path. These patterns of dye movements support the inferences from the thermistor data, which suggested that rippled beds in the flume induce relatively shallow exchange while the sediment column still retains a “basin-scale” flow path over the full length of the flume.

3.3.5. Trial 5: Rippled Bed Topography, 250L/min Flow Rate, 2.4mm Grain Size

Dye was injected at 11 points in the sediment column at various depths beneath a ripple train. Dye tracing results were similar to the 500L/min rippled bed test, but with stronger initial downward motion (which also visibly affected almost all of the injection points, including the shallowest points), and slower horizontal speeds. The size and shape of bedform-induced flow paths underneath the ripples was not affected by the change in flow rate, the speed of dye movement was less than the previous trial. Overall, this trial appeared to confirm the observations from the trial made at the higher flow rate.

3.3.6. Trial 6: Rippled Bed Topography, 125L/min Flow Rate, 2.4mm Grain Size

Dye was injected at 11 points in the sediment column at various depths beneath a ripple train. Dye spread rapidly downward in the first few minutes of the test. After the initial movement, further movement of dye consisted of very slow horizontal motion. Dispersion of dye also prevents the entire flow paths from being observed, since the time scales for flow through the subsurface were too long for the dye to pass through a full flow path without dissipating to a point where it could not be accurately tracked. These dye movement patterns indicate that bedform induced advection in this case is far less than that in the 500L/min and 250L/min rippled bed trials.

3.3.7. Trial 7: Plane Bed Topography, 500L/min Flow Rate, 2.4mm Grain Size

Dye was injected at 6 points in the sediment column, at shallow (<5 cm) and deep (>30 cm) depths. All dye injected exhibited rapid downward motion initially. Subsequently, some of the shallow dye arced upward to the bed, while some of the shallow dye continued to move diagonally downward, as did the dye injected at depths. The upward arcing motion is likely attributable to the small-scale irregularities in the bed inducing exchange (as discussed in 3.1.7.). Downward motion is attributable to density driven advection, as in prior trials. These dye movement patterns (i.e., the lack of the large arcing patterns from the rippled bed and pool-riffle-pool topographies) indicate that bedform induced advection in this case is minimal. This corresponds with results from the thermistor data.

3.3.8. Trial 8: Plane Bed Topography, 250L/min Flow Rate, 2.4mm Grain Size

Dye was injected at 6 points in the sediment column, at shallow (<5 cm) and deep (>30 cm) depths. All dye injected exhibited rapid downward motion initially. Subsequently, all dye exhibited diagonal downward motion, though at a steeper angle than in the 500L/min plane bed trial. Dye movement was less rapid than in the 500L/min plane bed trial, indicating slower hyporheic flows. These dye movement patterns (i.e., the lack of the large arcing patterns from the rippled bed and pool-riffle-pool topographies) indicate that bedform induced advection in this case is minimal. This corresponds with results from the thermistor data for the same trial.

3.3.9. Trial 9: Plane Bed Topography, 125L/min Flow Rate, 2.4mm Grain Size

Dye was injected at 6 points in the sediment column, at shallow (<5 cm) and deep (>30 cm) depths. All dye injected exhibited rapid downward motion initially, then moved slowly downstream. Dye movement was less rapid than in the 500L/min or 250L/min plane bed trials, indicating slower hyporheic flows. These dye movement patterns (i.e., the lack of the large arcing patterns from the rippled bed and pool-riffle-pool topographies) indicate that bedform induced advection in this case is minimal. This corresponds with results from the thermistor data for the same trial.

3.3.10. Trial 1: Pool-Riffle-Pool Topography, 500L/min Flow Rate, 6.4mm Grain Size

Dye was injected at 14 points in the sediment column upstream, downstream, and directly underneath the stoss and lee faces of the riffle. Dye tracing results corroborated

thermal studies. Dye patterns were almost identical to those in the corresponding trial at the smaller grain size. Dye injected upstream of the riffle crest moved in downward arcs, emerging at or near the riffle crest, while dye injected downstream of the riffle, or under its lee face, exhibited retrograde motion, emerging on the lee face of the riffle. Locations of downward and upward motion of dye corresponded with the locations of downwelling and upwelling zones inferred from the thermistor data. The only notable difference between this trial and Trial 1 is speed of dye motion. The larger grain size produced far greater hydraulic conductivities, and thus dye moved through the sediment at far greater speeds (up to 3 m/hr).

3.3.11. Trial 2: Pool-Riffle-Pool Topography, 250L/min Flow Rate, 6.4mm Grain Size

Dye was injected at 14 points in the sediment column upstream, downstream, and directly underneath the lower stoss and lee faces of the riffle. Dye tracing results corroborated thermal studies. Dye injected upstream of the riffle crest moved in downward arcs, emerging at or near the riffle crest, while dye injected downstream of the riffle, or under its lee face, exhibited retrograde motion, emerging on the lee face of the riffle. Patterns of dye motion were similar to those in the 500L/min test, but the dye moved less rapidly, especially in the secondary downwelling zone downstream of the riffle, though still more rapidly than in the trials conducted with the smaller sediment sizes. Locations of downward and upward motion of dye corresponded with the locations of downwelling and upwelling zones inferred from the thermistor data, as in the previous trial.

3.3.12. Trial 3: Pool-Riffle-Pool Topography, 125L/min Flow Rate, 6.4mm Grain Size

Dye was injected at 15 points in the sediment column upstream, downstream, and directly underneath the lower stoss and lee faces of the riffle. Dye spread rapidly downward in the first few minutes of the test, presumably due to the same effects proposed in earlier trials with the smaller sediment. After a few minutes, the dye began to equilibrate with the surrounding water and normal advective motion resumed. With smaller sediment, advective flow generated from a 125L/min stream flow rate was not enough to significantly affect the subsurface, and the flow paths were not clear. With the larger grain sizes used in this trial, dye motion allowed visualization of flow paths, which were similar to those in previous pool-riffle-pool trials. However, dye did not move as rapidly as in Trials 10 and 11, as would be expected based on the lower flow rate.

3.3.13. Trial 4: Rippled Bed Topography, 500L/min Flow Rate, 6.4mm Grain Size

Dye was injected at 10 points in the sediment column at various depths beneath a ripple train. Dye injected at shallow depths under the lee face of a ripple, or under the base of the trough, exhibited retrograde motion toward the crest. Dye injected on the lower stoss face of the ripple exhibited clear downwelling, reaching its greatest depth (~20cm) underneath the ripple crest, before rising on the lee face. Some of the deeper injection points resulted in slower horizontal flow, indicating that advective flow was generally horizontal below a shallow region in which the ripples induced significant exchange. Advective motion was strong enough that the effect of dye sinking in the initial minutes of the trial was negligible, unlike in Trial 4. These patterns of dye movements support the

inferences from the thermistor data, which suggested that rippled beds in the flume induce relatively shallow exchange while the sediment column still retains a “basin-scale” flow path over the full length of the flume.

3.3.14. Trial 5: Rippled Bed Topography, 250L/min Flow Rate, 6.4mm Grain Size

Dye was injected at 10 points in the sediment column at various depths beneath a ripple train. Dye tracing results were similar to the previous trial, but with significantly slower dye movement. The shape and size of the observed flow paths was approximately the same as in the prior trial. Overall, this trial appeared to confirm the observations from the trial made at the higher flow rate.

3.3.15. Trial 6: Rippled Bed Topography, 125L/min Flow Rate, 6.4mm Grain Size

Dye was injected at 10 points in the sediment column at various depths beneath a ripple train. Dye spread rapidly downward in the first few minutes of the test. After the initial movement, further movement of dye consisted of very slow horizontal and diagonally downward motion at the lower depths, while dye close to the surface followed the patterns established in the 500L/min and 250L/min trials. Dispersion of dye prevented observation of the entire length of some flow paths, since the time scales for flow through the subsurface were too long for the dye to pass through a full flow path without dissipating to a point where it could not be accurately tracked. These dye movement patterns indicate that bedform induced advection in this case is far less than that in the 500L/min and 250L/min rippled bed trials at the same grain size.

3.3.16. Trial 7: Plane Bed Topography, 500L/min Flow Rate, 6.4mm Grain Size

Dye was injected at 6 points in the sediment column, at shallow (<5 cm) and deep (>30 cm) depths. All dye injected exhibited diagonally downward motion in the downstream direction. Downward motion may be partially attributable to density driven advection, as in prior trials. These dye movement patterns (i.e., the lack of the large arcing patterns from the rippled bed and pool-riffle-pool topographies) indicate that bedform induced advection in this case is minimal. This corresponds with results from the thermistor data and expectations for a plane bed. There was no evidence of bedform-driven advection as the result of small surface irregularities, as there was in Trial 7.

3.3.17. Trial 8: Plane Bed Topography, 250L/min Flow Rate, 6.4mm Grain Size

Dye was injected at 6 points in the sediment column, at shallow (<5 cm) and deep (>30 cm) depths. All dye injected exhibited rapid downward motion initially. Subsequently, all dye exhibited diagonal downward motion, though at a steeper angle than in the 500L/min plane bed trial. Dye movement was less rapid than in the 500L/min plane bed trial, indicating slower hyporheic flows. These dye movement patterns indicate that bedform induced advection in this case is minimal, as has been observed in the other plane bed trials.

3.3.18. Trial 9: Plane Bed Topography, 125L/min Flow Rate, 6.4mm Grain Size

Dye was injected at 6 points in the sediment column, at shallow (<5 cm) and deep (>30 cm) depths. All dye injected exhibited rapid downward motion initially, then moved

slowly downstream. Dye movement was less rapid than in the 500L/min or 250L/min plane bed trials, indicating slower hyporheic flows. At two of the shallow injection points, dye moved in a small upward arc, contrary to previous trials and expectations for a plane bed. These results may be anomalous, or may be the result of some disturbance in the bed (e.g., from adjusting the thermistor rods). While the dye did exhibit rapid downward motion initially, it did not sink as much as in the prior two trials. Overall, the results still suggest minimal bedform-induced exchange, so despite the discrepancies with the previous trials the dye traces still support the results from the thermistor data.

3.4. SUMMARY OF DYE TRACING TEST RESULTS

Dye tracing tests generally corresponded to results of the temperature dynamics trials. Observations of flow patterns conformed to predicted flow paths modeled by Cardenas and Wilson (2007b). In trials 1-3 and 10-12 (pool-riffle-pool) dye injected under the stoss face of the riffle moved in a concave-up curve, emerging at or near the riffle crest. Dye injected further from the crest typically penetrated further into the sediment column, and emerged slightly further downstream than dye injected closer to the crest. Dye injected on the lee face of a riffle generally moved slightly upstream toward the crest, or was immediately expelled from the lee face. Dye injected slightly downstream of the riffle generally followed a concave up course toward the lee face (opposite to prevailing flow direction), but moved slowly relative to injections in the stoss face. Higher flow rates and larger grain sizes resulted in more rapid dye movement, with increasing the grain size having a substantially greater effect relative to increasing the flow rate. However, shape

and depth of flow paths were not affected by grain size or flow rates. Presumably, the fact that higher flow rates and larger grain sizes induce deeper penetration of temperature signals is due to variations in the magnitude of hyporheic fluxes, rather than variations in the location and depth of those fluxes.

Dye tracing tests in trials 4-6 and 13-15 (rippled bed) produced patterns nearly identical to those in the pool-riffle-pool trials, though on a smaller scale. The primary differences between the flow paths induced by the two bedform regimes are that in the case of the ripple train, the hyporheic flow paths moving opposite to the prevailing streamflow were generally minimized, and dye emergence tended to occur on the lower lee face rather than at the bedform crest. Presumably, these differences are attributable to the effect of adding additional bedforms in sequence, and not to scaling factors, as flow patterns were otherwise very similar between the two bedform sizes.

Dye tracing tests in trials 7-9 and 16-18 (plane bed) generally resulted in stagnant dye patterns, with some horizontal patterns. Dye also tended to sink in the first few minutes of tests, possibly due to differences in dye temperature and density relative to the flume water. This was the case in several trials, but was most noticeable in the plane bed trials where advective motion was small. Upward motion was generally minimal in these trials.

4. Discussion

4.1. THERMAL DYNAMICS OF BEDFORM-INDUCED HYPORHEIC EXCHANGE

These results demonstrate that bedforms induce significant thermal heterogeneity within the hyporheic zone. Observed thermal patterns are scaled with bedform size, and the magnitude of advective heat flow increases along with flow rate and permeability. More specifically, examination of amplitude ratios and dye tracing paths in the ripple and pool-riffle-pool trials suggests that the bedforms within the flume generate hyporheic flow paths reaching roughly 0.5 bedform wavelengths into the sediment. This is an approximation; it holds true for the ripples (dye trace curves reach about 25cm in depth, and at 30 cm and below the temperature signals no longer form a clear pattern of upwelling and downwelling for each ripple), while for the pool-riffle-pool system such a depth of penetration (~1m for a 2m long bedform) would result in flow paths intersecting the base of the sediment column, which is clearly not possible. However, the dye tracing tests and thermal advection studies do suggest that advective transport generated by pool-riffle-pool topography reaches the base of the sediment column, so a ~1m depth might occur in a deeper sediment column. The depth appears to be correlated with the wavelength of the bedform, rather than its height. If depth of flow paths was correlated with bedform height, the pool-riffle-pool system would have flow paths of roughly double the depth of those generated by the rippled bed (the ripples and the riffle are not similar in shape), rather than quadruple the depth as predicted by a length correlation. In this case, exchange processes

generated by the pool-riffle-pool topography would only affect the uppermost ~0.5m of the sediment column, but observations indicate that they affect the entire column. Thus, I conclude that depth of hyporheic exchange flow paths generated by a bedform is most closely correlated with wavelength of the bedform, and that a rough estimate of the depth of the hyporheic zone is 0.5λ , where λ = bedform wavelength.

The shape and size of dye-traced flow paths did not vary between flow paths or sediment sizes; these variables affected only the subsurface flow velocities. This indicates that increased hyporheic exchange generated by changing the flow rate or sediment size is not caused by deeper penetration of hyporheic flow paths; instead, increased hydraulic conductivity (in the case of changing sediment size) and increased hydraulic head (in the case of changing flow rate) seem to be the driving factors in increasing hyporheic fluxes. Flow path shapes and depths are only altered by changing the bedform topography, not by changing the sediment size or flow rate. Thermal advection, however, will also be controlled by both depth of penetration and magnitude of fluxes, so overall heat fluxes are more difficult to predict, as they will depend on all three factors.

Magnitude of thermal advection appears to be directly correlated to channel flow rates. For example, in Trials 1-3 (2.4mm grain size, pool-riffle-pool topography), there appears to be a linear relationship between amplitude ratios in the downwelling zone and flow rates. At 50cm depth, the amplitude ratios corresponding to 500L/min, 250L/min and 125L/min are approximately 0.8, 0.4, and 0.2 respectively, indicating a direct relationship between the two. A similar variation is observed at 20cm depth (approximately 1.0, 0.8,

and 0.4 for 500L/min, 250L/min and 125L/min flow rates respectively), as well as in ripple downwelling zones (somewhat variable, but at 20cm depth on average about 0.8, 0.6, and 0.4 for 500L/min, 250L/min and 125L/min flow rates respectively). Amplitudes in the large grain size trials were far greater, preventing proper analysis of flow rate effects. Variation in the upwelling zones is far less, ranging with amplitude ratios for 500L/min, 250L/min and 125L/min flow rates of approximately 0.3, 0.1, and 0.1 respectively. Amplitude ratios represent the proportion of the stream temperature profile that is transmitted to a given depth, so this indicates that channel flow rate is a strong controlling factor on temperature patterns for the downwelling zone, but a minor factor in controlling upwelling zone temperatures (which is expected, since upwelling zones are dominated by thermally stable groundwater).

The results from this study also demonstrate a strong connection between permeability and the magnitude of thermal advection. Increased amplitude ratios were observed at nearly all locations within the flume during trials with the 6.4mm grain size relative to the corresponding 2.4mm grain size trials at the same flow rates and bedform topographies (compare Figure 3.1.1 with 3.1.10, 3.1.2 with 3.1.11, etc.). Permeability varied by roughly one order of magnitude between the two grain sizes ($3.4 \times 10^{-9} \text{ m}^2$ for the 2.4 mm sediment and $3.3 \times 10^{-8} \text{ m}^2$ for the 6.4 mm sediment). However, it is difficult to tell whether a similar variation in magnitude of thermal advection occurred, as the permeability was so high that for several of the tests the entire temperature signal was transmitted through almost all of the sediment. The increased permeability certainly increases thermal

advection, but the relationship between the two is unclear – in the plane bed and rippled bed cases, amplitude ratios are far higher than with the smaller sediment, while in the pool-riffle-pool cases, amplitudes ratios only increase slightly (generally 0.1-0.2). However, I can safely conclude that increasing permeability does increase thermal exchange to at least some extent, even if the exact nature of that relationship is uncertain.

These findings support predictions obtained by modeling by Cardenas and Wilson (2007b) and Sawyer et al. (2012) that increased permeability and flow rate induce greater total hyporheic exchange. Since permeability is observed to have a direct impact on the magnitude of thermal advection, reduction in permeability (e.g., by pore clogging or changes in sediment type) will likely reduce hyporheic exchange and thermal heterogeneity in the hyporheic zone. Similarly, increased exchange is likely to occur when flow rates increase (e.g. as a result of flooding), regardless of the permeability or bedform topography.

Previous studies by Sawyer et al. (2012) using similar conditions (logs as the flow-obstructing object, rather than bedforms), found that some observed temperatures oscillated at multiple frequencies in shallow upwelling zones. I observed no such anomaly in observed temperature patterns during my study. The bedforms did increase complexity of temperature signals, most notably in the rippled bed trials, which involved multiple bedforms. However, this complexity was insufficient to cause changes in frequency. Temperature oscillations remained diel in frequency throughout the sediment (reflecting the behavior of surface water), although the idealized sinusoidal cycles imposed in the surface water were not preserved. Due to the number of trials run in this experiment, I

suggest that the multiple frequencies arising in earlier experiments may be anomalous, or may be confined to a very specific set of circumstances.

For the purposes of this study, I did not include net groundwater discharge as a variable. Most streams are either gaining or losing, so this is a significant simplification, since both net groundwater fluxes can strongly influence the expected temperature patterns within the hyporheic zone (Cardenas and Wilson 2007c), as is the use of an insulative basal boundary. The insulative basal boundary, along with insulation on the walls of the flume, is intended to minimize temperature fluxes across all the boundaries of the sediment column, apart from the bed. Thus, ambient temperature fluctuations outside the flume are theoretically prevented from impinging upon the sediment column, so that all temperature fluctuations within the sediment can be assumed to have been generated by hyporheic flow. In natural systems, mean temperatures of stream water and groundwater are generally unequal, resulting in a gradient of mean temperatures across the hyporheic zone. This effect could be replicated by applying a heating or cooling element to the flume base to represent groundwater. As noted in prior studies with this flume (Sawyer et al. 2012) installing a heating or cooling element would not change the amplitude and phase lag distributions within the hyporheic zone, though this action would affect their magnitudes (i.e., heating or cooling elements may cause temperatures amplitudes to decay faster or slower with increasing depth, but they should change uniformly in the longitudinal direction). In a zero-net groundwater flux system, with constant basal groundwater temperature, within typical temperature ranges, thermal advection and conduction at the

bottom of the hyporheic zone should be minimal, relative to hyporheic exchange fluxes. Thus, a constant temperature basal boundary should be a good approximation of at least some natural systems.

Similar flume studies have been conducted with ripple trains alone (Janssen et al. 2012) and flow obstructions such as large woody debris (Sawyer et al. 2012, Mutz et al. 2007). Additionally, field studies have been conducted assessing in stream-riffles (Swanson and Cardenas 2010), weirs, and other elements of natural river systems. Flume studies can never fully replace dedicated field studies, as there are too many variables in a natural system. Stream temperature dynamics, for example, will never take the pattern of a simple sinusoid over extended periods, as this approximation excludes the complex dynamics of solar heating, cloud cover, groundwater fluxes, and riparian shading. A few natural systems, however, may be closely analogous to the flume (e.g., a grassland stream where cloud cover is minimal and poor land management practices have resulted in destruction of riparian vegetation). Similarly, dynamic bedforms cannot be studied using my techniques, and heterogeneous and anisotropic sediments have not been considered. In natural systems, anisotropy has been shown to have a strong effect on hyporheic flow (Zlotnik et al. 2011), so these results will be most applicable to homogenous, isotropic sediments. While flume studies cannot replicate field conditions, they provide an acceptable analogue while allowing direct control of multiple parameters. To my knowledge, this is the first flume study that addresses the impact of bedforms on hyporheic temperature patterns while directly controlling for four primary stream variables

(temperature, flow rate, bedform regime, and permeability), and the first to assess multiple bedform types.

4.2. POSSIBLE LINKAGES BETWEEN HYPORHEIC ZONE AND CATCHMENT SCALE PROCESSES

From these results I can infer how a stream's hyporheic zone may respond to changes in stream and streambed characteristics. If geomorphological changes induce a change in bedform regime or a change in sediment size, or if streamflow changes, the volume of hyporheic exchange and the magnitude and location of thermal heterogeneity will be influenced by these changes.

By extension, researchers may infer possible effects of many characteristics of a watershed on the stream environment by linking hyporheic-exchange processes directly to sediment transport processes and fluvial geomorphology. Working from known data about erosion rates, runoff, and other factors, it is already possible to develop models describing how the bedform regimes of a stream will be affected by changes to these parameters. Much work has been done establishing how to use bedforms to determine whether a system is supply-limited or transport-limited, and how to determine overall sediment budgets based on a stream's bedform regime (Einsele 2000, Church 2006). Conversely, characteristics of the catchment (e.g. vegetation cover, erosion rates, runoff, etc.) can be used to make predictions about downstream channel form and bedform regimes (Simons and Richardson 1966, Simons and Senturk 1992). Since changes to bedform regimes result in substantial changes to thermal heterogeneity patterns and magnitudes of hyporheic exchange, the effects of basin-scale processes on hyporheic zones in individual reaches

should be calculable. As researchers further explore the biogeochemical ramifications of hyporheic exchange processes, they may be able to determine how these processes will be affected by changes to basin-scale parameters.

4.3. POTENTIAL BIOLOGICAL AND CHEMICAL IMPLICATIONS OF THERMAL HETEROGENEITY VARIATION DUE TO CHANGING BEDFORM REGIMES

Linkages between basin-scale processes, bedform regimes, hyporheic zone processes (including heat transport), and biogeochemical processes result in substantive chemical and biological implications. Temperature sensitive organisms living at the stream/groundwater interface, but within a bedform-induced upwelling zone (a stable temperature zone), would be negatively impacted by a transition to a plane bed system, as they would be exposed to greater temperature variation in the new environment. Organisms living in downwelling zones may benefit from increased nutrient and oxygen fluxes. In such cases, the very existence of a bedform regime results in increased habitat availability by providing thermal heterogeneity within the sediment column. Removal of these bedforms might translate directly to the loss of thermal refugia for organisms within the hyporheic zone. Habitat loss from bedform removal might not be considered in traditional assessments of land use impacts on streams, but might have non-trivial repercussions for the aquatic ecosystem.

Bedform regime changes may have chemical implications as well as biological ones. This study suggests that a transition from a plane bed to a rippled bed due to increased sediment load is likely to induce increased hyporheic fluxes at depth, resulting

in greater variation of physical and chemical parameters (temperature, pH, DO, etc.) at greater depths. In a stream with a layer of contaminated sediment some distance beneath the bed (e.g., residual metals deposited from mine drainage), increased burial might be assumed to be beneficial. However, if increased aggradation of sediment results in the formation of new bedforms, the deep flow paths associated with these bedforms could draw pollutants out through upwelling zones, resulting in sudden release of contaminants into the stream, perhaps one that has been ostensibly remediated and does not typically exceed water quality criteria. My results suggest that such flow paths may reach depths of roughly half a bedform wavelength, which in some rivers could be several meters or more. As noted in the introduction, temperature (and pH) variations may affect metal cycling processes, so hyporheic exchange and associated temperature and pH cycles could increase variation in of metal concentrations, rendering contaminant measurements incorrect. This will be true for temperature dependent processes as well as pH dependent processes, as pH increases in streams are photosynthetically induced and thus, like temperature variations, are controlled primarily by solar radiation (Jones et. al. 2003). In either case, bedform-induced hyporheic flow will transport reactive water into the streambed. Bedform-induced hyporheic exchange may flush free contaminants into the stream on its own, or induced thermal heterogeneity may result in thermally induced desorption of metals, which can then be carried back to the surface.

5. Conclusions

Bedforms induce significant thermal heterogeneity within the hyporheic zone at scales corresponding to the size of the bedforms. Thermal heterogeneity increases with increasing bedform size, sediment permeability, and channel flow rates. When comparing different streams, permeability is likely to be the dominant factor in controlling hyporheic exchange and heat flux, as it varies by several orders of magnitude more than either bedform size or channel flow rates. Within individual reaches, however, where sediment size (and therefore permeability) may be less likely to undergo drastic changes, streambed topography (and changes thereto) may also control this exchange. Bedform regimes may change along with variations in the overall sediment budget; consequently, changes to hyporheic exchange and thermal flux rates may be unintended side effects of erosional loading or other alterations to the sediment budget of a given reach. These changes may also impact permeability and flow rates, further altering thermal patterns within the hyporheic zone. Since thermal heterogeneity induced by bedforms may impact both streambed ecology (by increasing habitat complexity and forming thermal refugia for organisms) and streambed chemistry (by affecting denitrification, metal cycling, and other processes), changes to bedform topography have the potential to adversely alter a stream's ecosystem or chemistry. This study suggests that bedforms may induce exchange at up to half a bedform wavelength, which may pose a significant threat to streams containing sensitive organisms or shallowly buried pollutants. It also indicates that any increase in flow velocity is likely to cause a proportional increase in total hyporheic exchange. Though

the flow paths will not increase in depth with increasing flow velocities, the total heat transferred to a given depth within the hyporheic zone will increase. Further study on this subject should examine direct coupling of heat transport and reactive chemical transport to determine if such changes could result in detrimental effects to stream ecosystems and human health, particularly in streams being rehabilitated from contamination.

Appendix: Figures

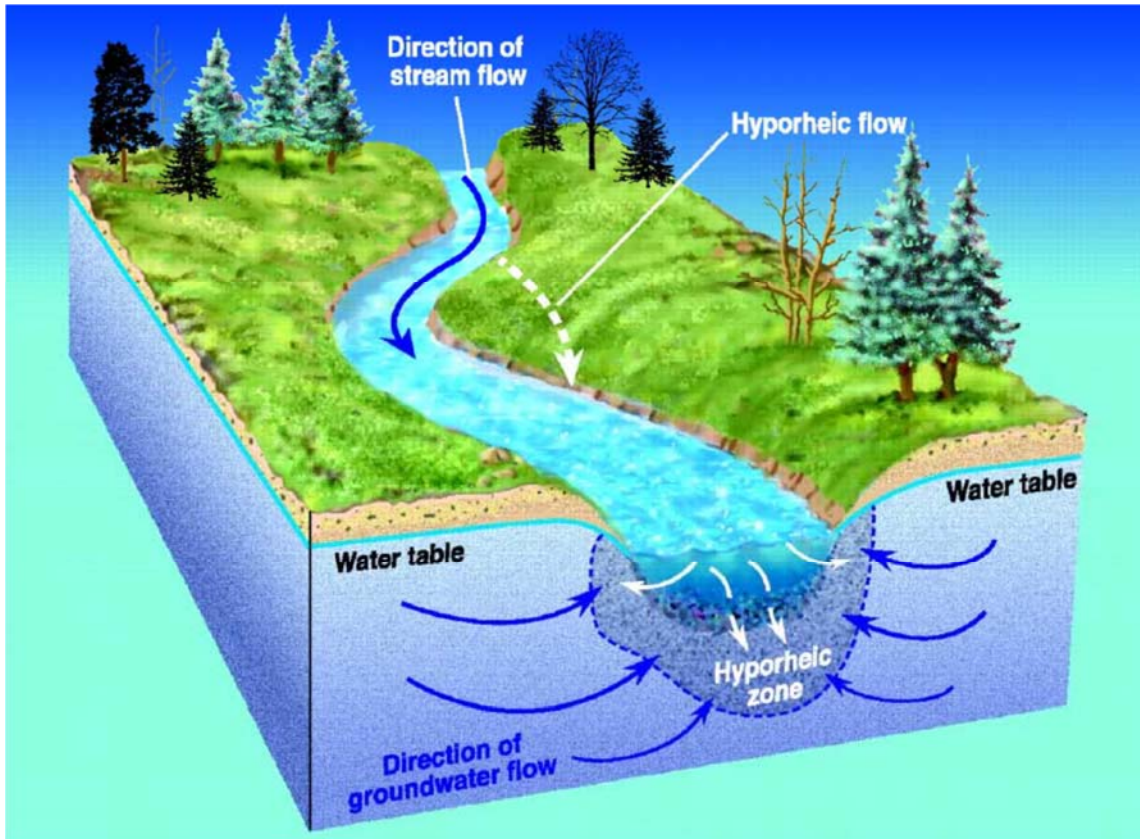


Figure 1.a. Groundwater system involving the hyporheic zone, from Alley et al. (2002).

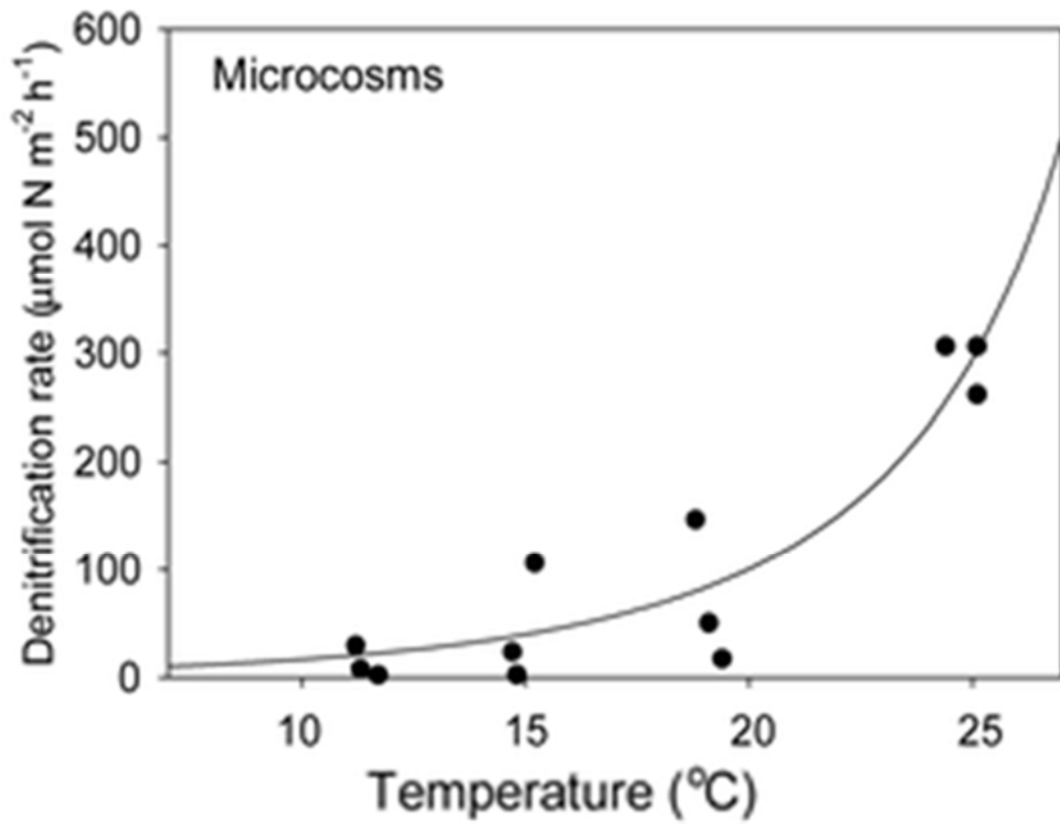


Figure 1.b. Temperature dependence of denitrification. From Veraart et al. (2011)

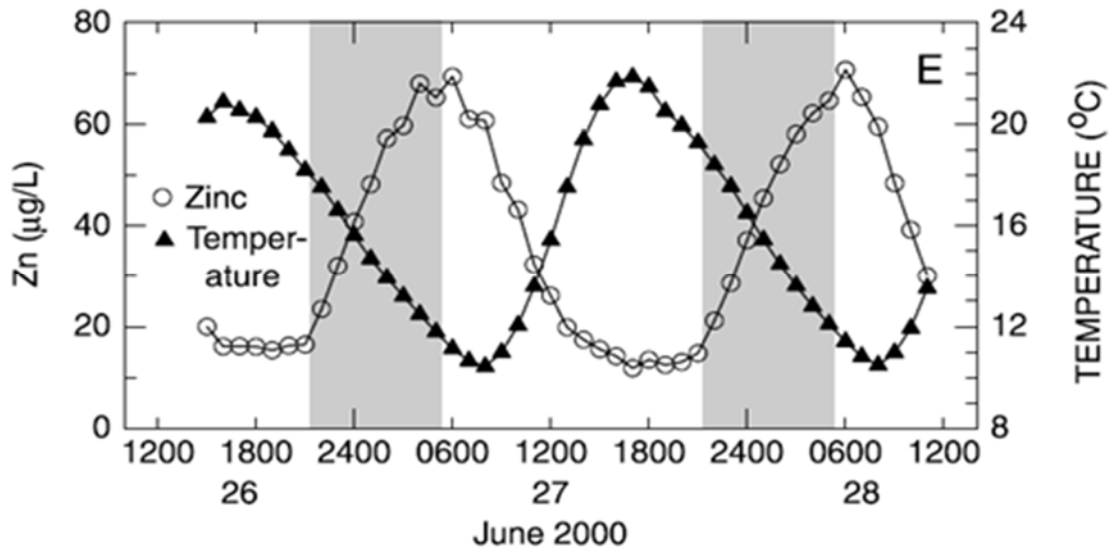


Figure 1.c. Concurrent diel variation of zinc concentrations and temperatures in Prickly Pear Creek, MT, 26-28 June 2000. Shaded areas indicate nighttime hours. From Nimick et al. (2003).

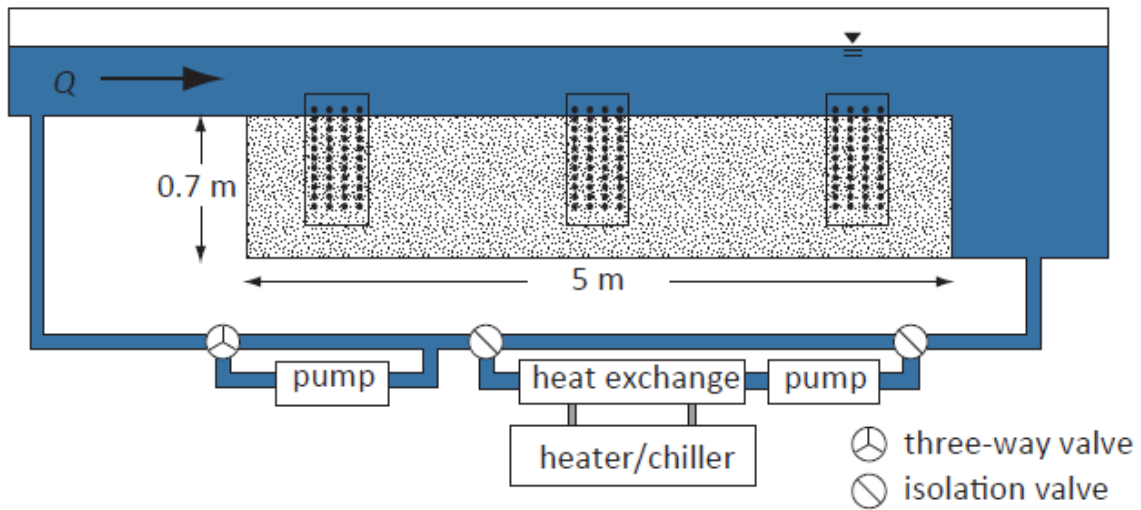


Figure 2.1.a. Schematic diagram of laboratory flume. Stippled area represents the sediment column, with the 3 panels of gridded points representing dye injection ports, and the blue region representing the “stream” of recirculating water.



Figure 2.1.b. Image of flume with fiberglass insulation in place to minimize heat conduction through flume walls.



Figure 2.2.1.a. Image of flume with pool-riffle-pool bedform in place, with smaller (2.4mm) sediment. The riffle is 200 cm long and 15 cm high. Dye injection ports can be seen in far right panel of the flume, and the second panel from the left.



Figure 2.2.1.b. Image of flume with rippled bed topography in place, with smaller (2.4mm) sediment. Ripples are 50 cm long and 7.5cm high.



Figure 2.2.1.c. Image of flume with flat bed topography in place, with smaller (2.4mm) sediment. Ripples are 50 cm long and 7.5cm high.

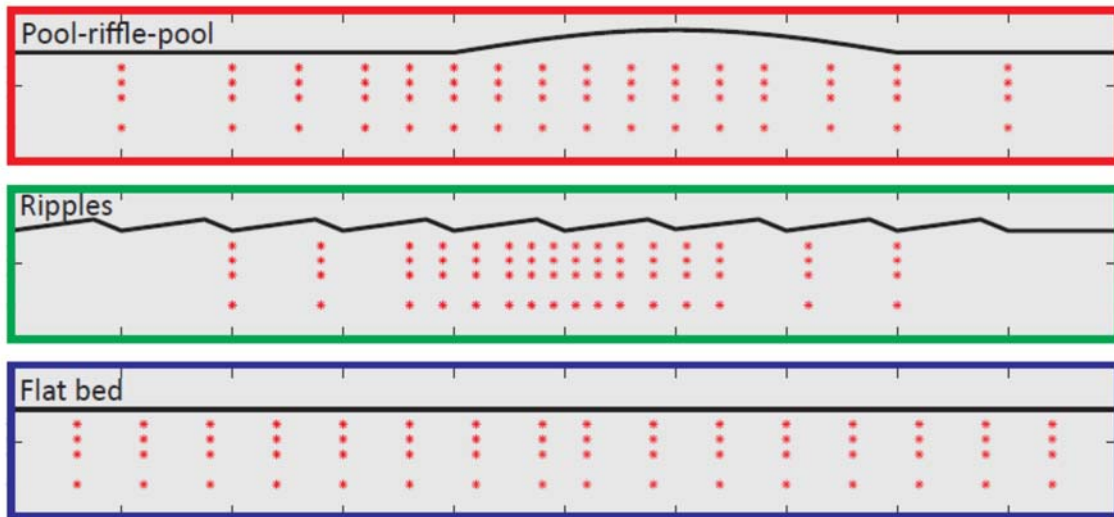


Figure 2.4.a. Thermistor Arrays for each bedform size. The thick black line represents the stream bed, and the red points indicate thermistor locations. Hashes around the edges are at 0.5m intervals. Different thermistor spacing was used for different bedform types. For the flat bed, a uniform spacing was used, but for the other two bedforms the thermistors were spaced more closely at the center of the sediment column, in order to analyze the downwelling zones with greater precision.

Thermistor depths are 10, 20, 30, and 50 cm below the flat bed surface, and at corresponding elevations for the other two bedform topographies. Total sediment column depth was 72cm, so this corresponds to elevations of 22, 42, 52, and 62 cm above the base of the sediment column for each group of thermistors.

Horizontal location of thermistors for each bedform topography is as follows (from left to right):

Pool-Riffle-Pool: 0, 50, 100, 130, 160, 180, 200, 220, 240, 260, 300, 230, 240, 370, 400, 450, and 500 cm.

Ripples: 0, 100, 140, 180, 195, 210, 225, 235, 245, 255, 265, 275, 290, 305, 320, 360, 400, and 500 cm.

Flat Bed: 0, 30, 60, 90, 120, 150, 180, 210, 240, 260, 290, 320, 350, 380, 410, 440, 470, and 500 cm.



Figure 2.4.b. Flume with HOBO U12 data loggers. Each data logger is records one column of four thermistors.

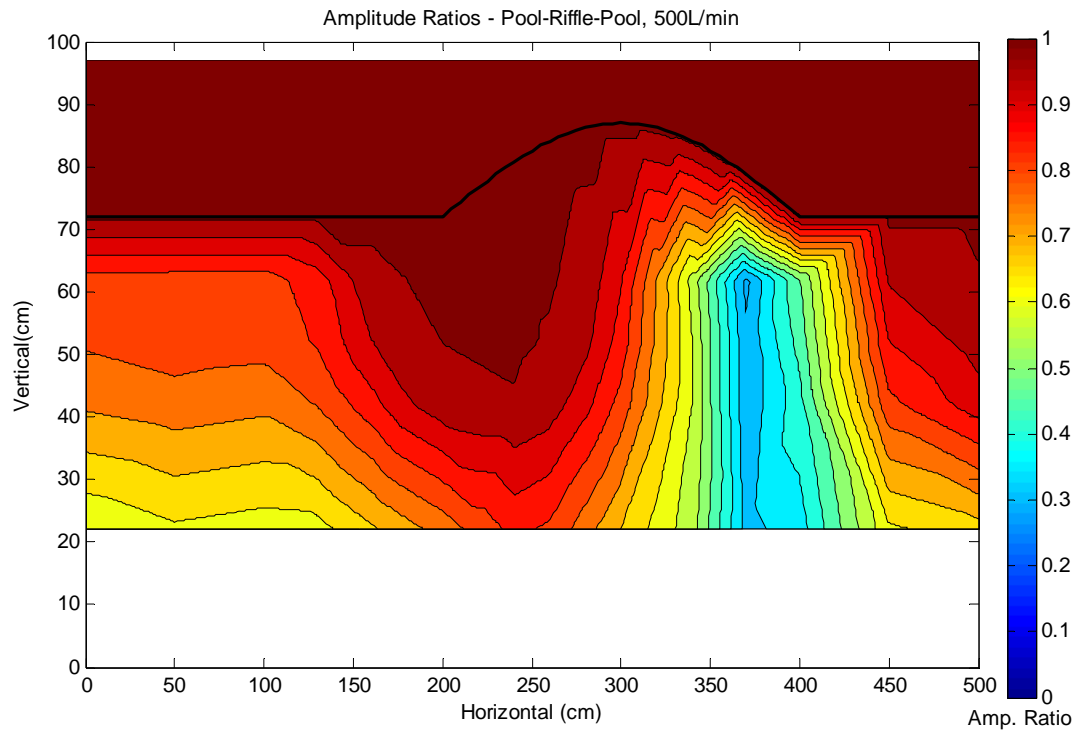


Figure 3.1.1. Temperature Amplitude Ratios, Trial 1: Pool-Riffle-Pool Topography, 500L/min Flow Rate, 2.4mm Grain Size

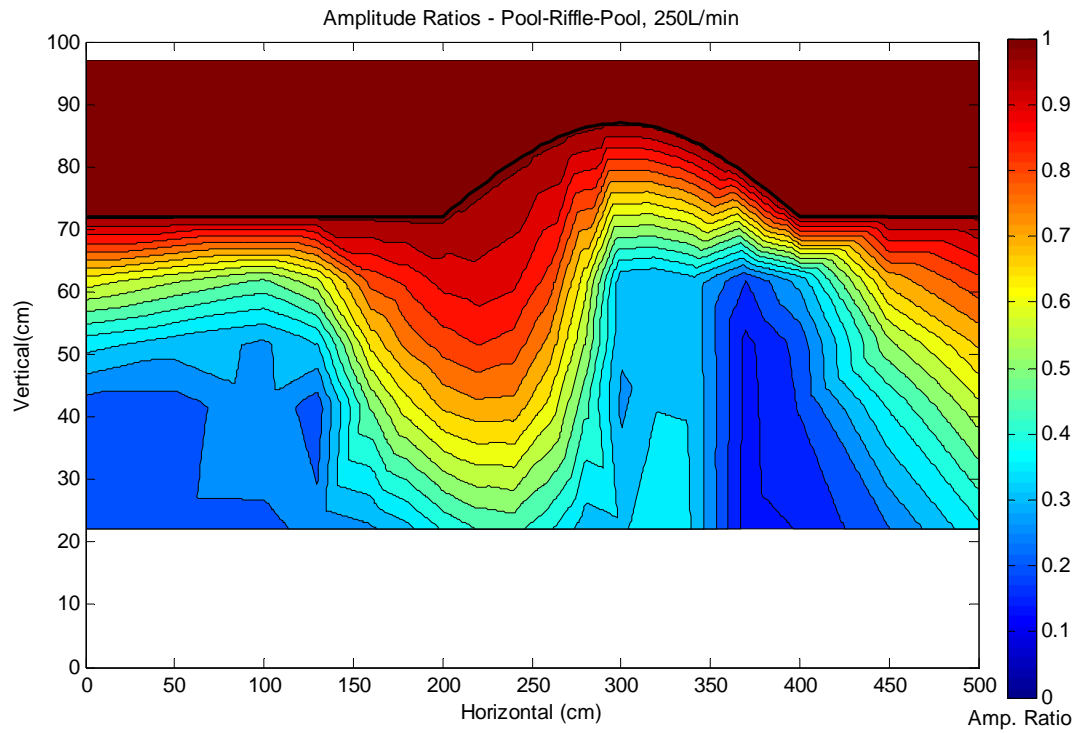


Figure 3.1.2. Temperature Amplitude Ratios, Trial 2: Pool-Riffle-Pool Topography, 250L/min Flow Rate, 2.4mm Grain Size

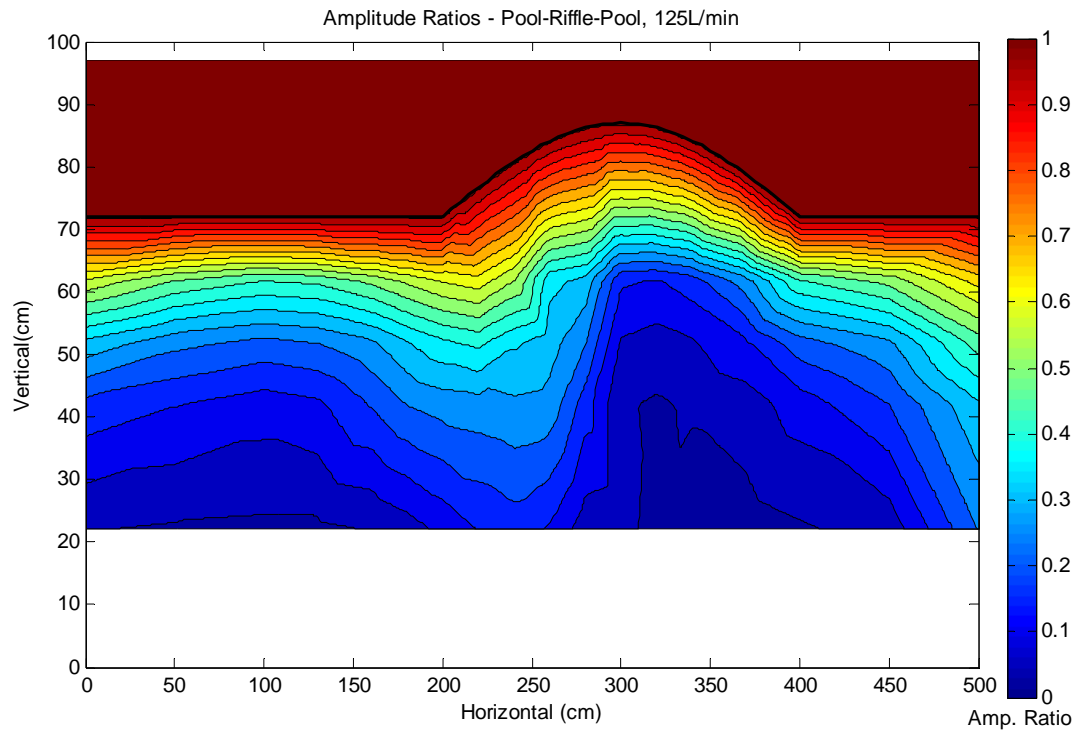


Figure 3.1.3. Temperature Amplitude Ratios, Trial 3: Pool-Riffle-Pool Topography, 125L/min Flow Rate, 2.4mm Grain Size

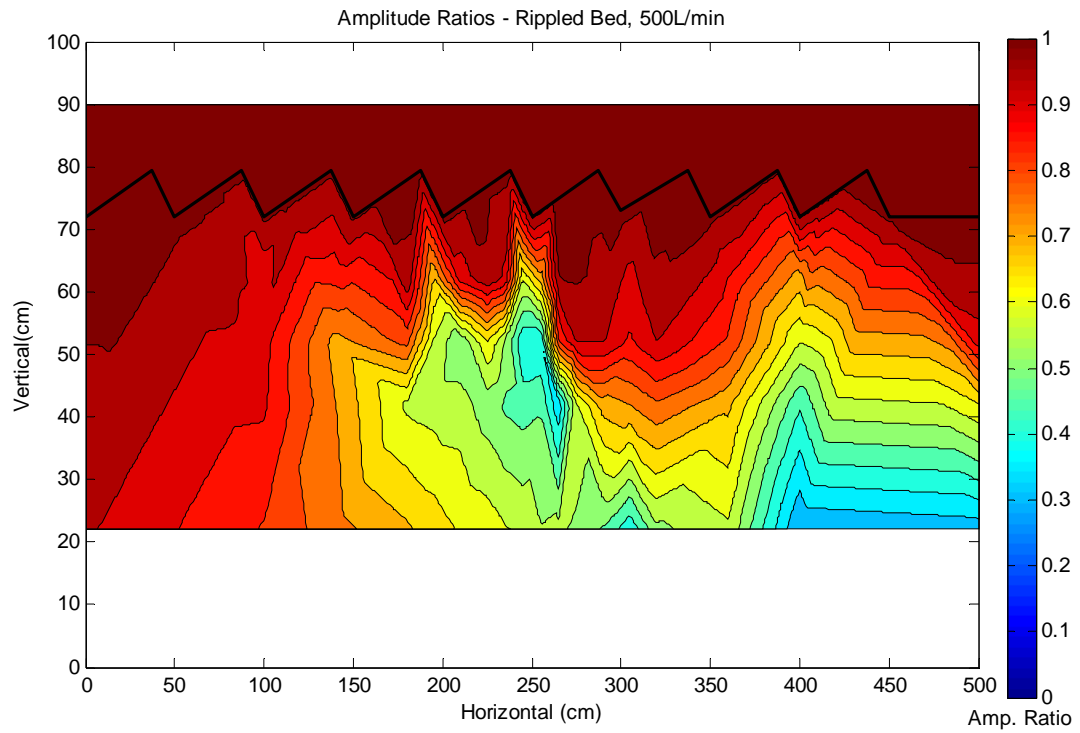


Figure 3.1.4. Temperature Amplitude Ratios, Trial 4: Rippled Bed Topography, 500L/min Flow Rate, 2.4mm Grain Size

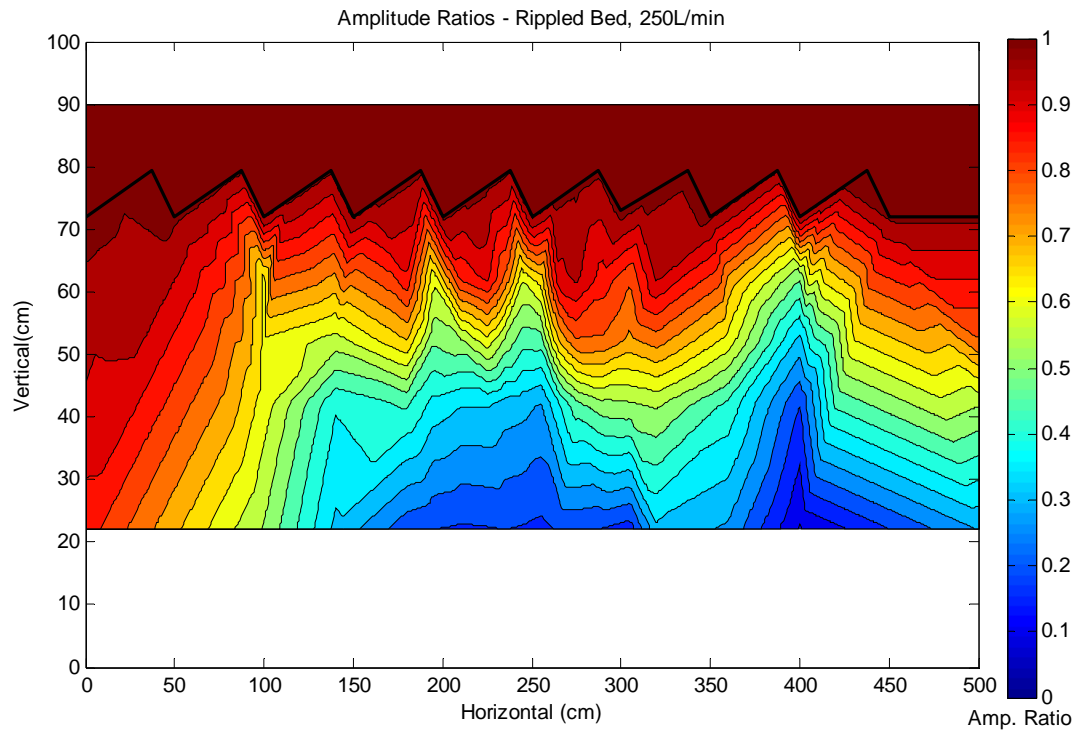


Figure 3.1.5. Temperature Amplitude Ratios, Trial 5: Rippled Bed Topography, 250L/min Flow Rate, 2.4mm Grain Size

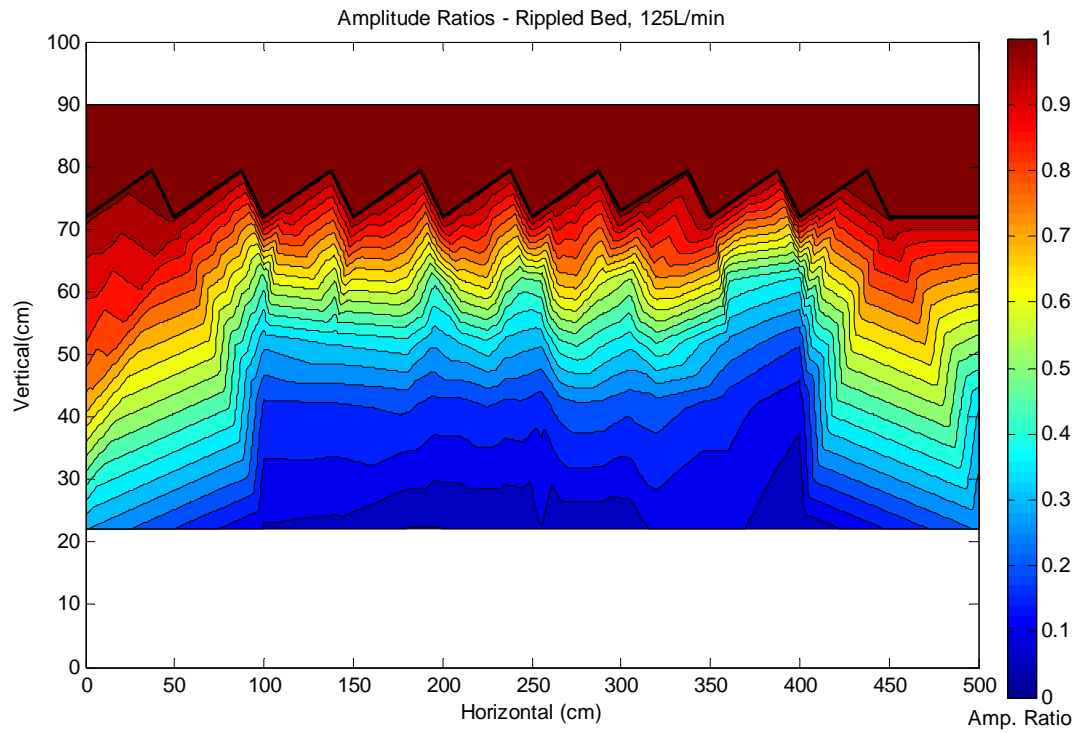


Figure 3.1.6. Temperature Amplitude Ratios, Trial 6: Rippled Bed Topography, 125L/min Flow Rate, 2.4mm Grain Size

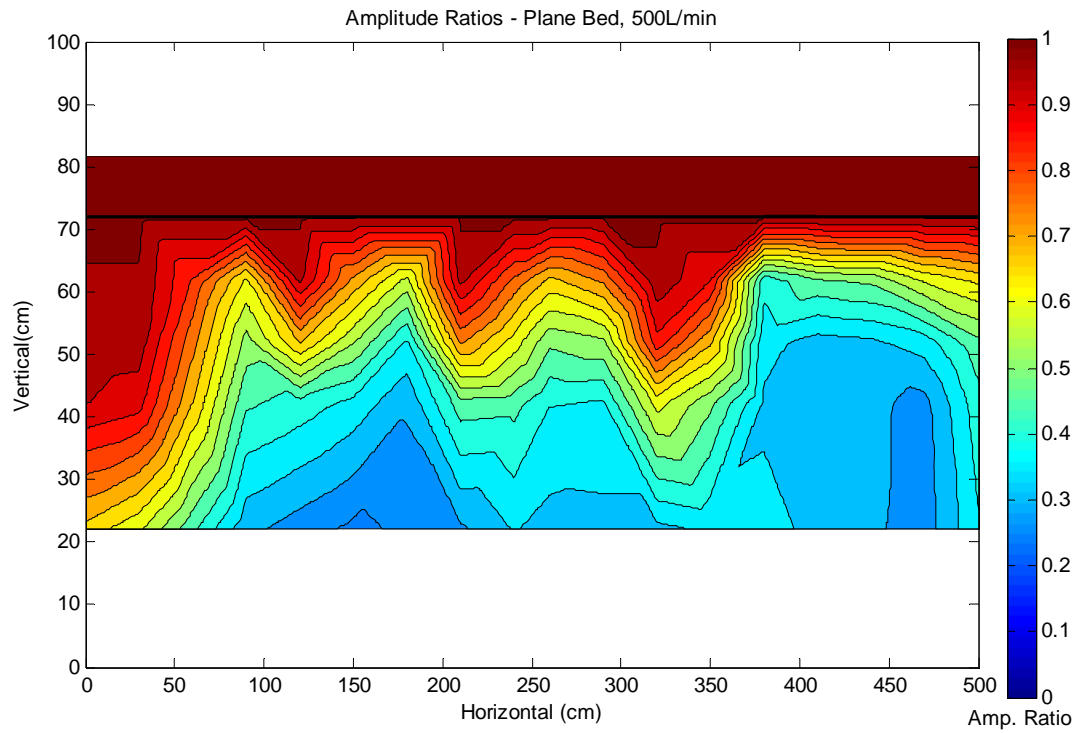


Figure 3.1.7. Temperature Amplitude Ratios, Trial 7: Plane Bed Topography, 500L/min Flow Rate, 2.4mm Grain Size

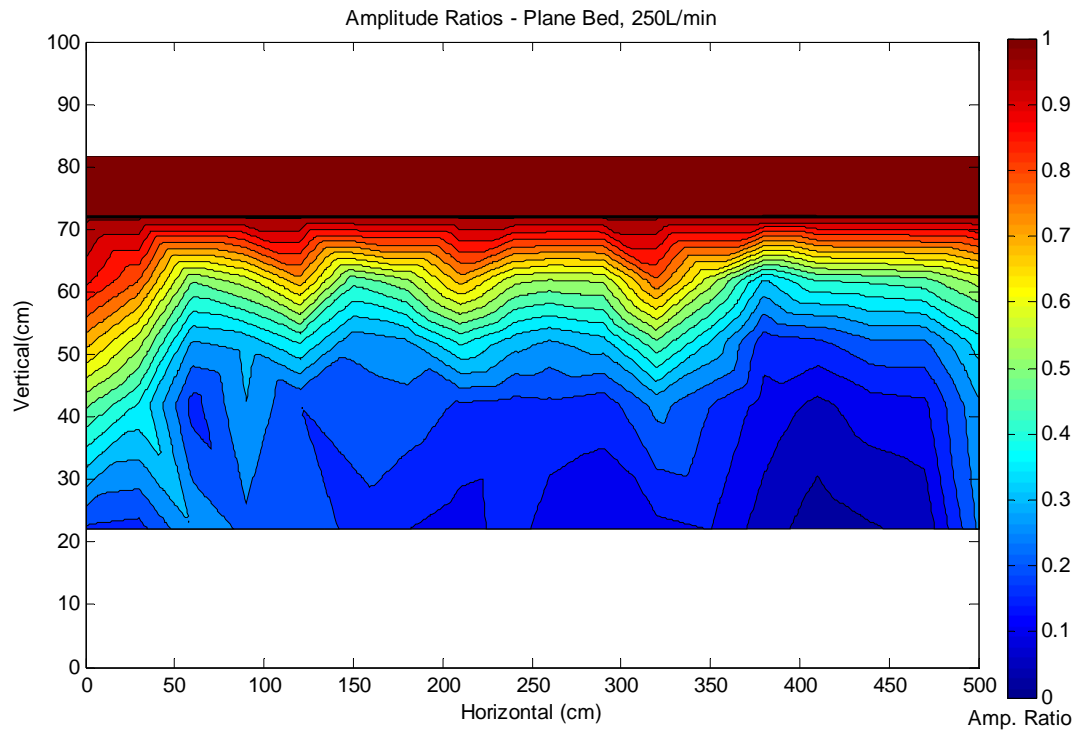


Figure 3.1.8. Temperature Amplitude Ratios, Trial 8: Plane Bed Topography, 250L/min Flow Rate, 2.4mm Grain Size

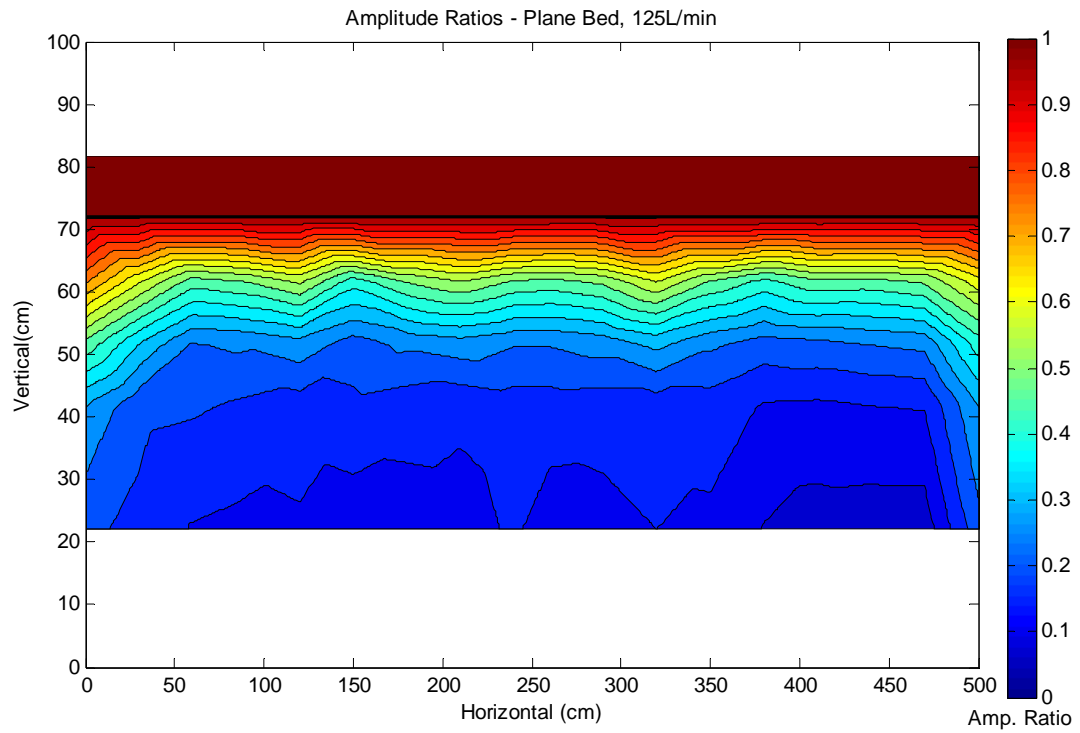


Figure 3.1.9. Temperature Amplitude Ratios, Trial 9: Plane Bed Topography, 125L/min Flow Rate, 2.4mm Grain Size

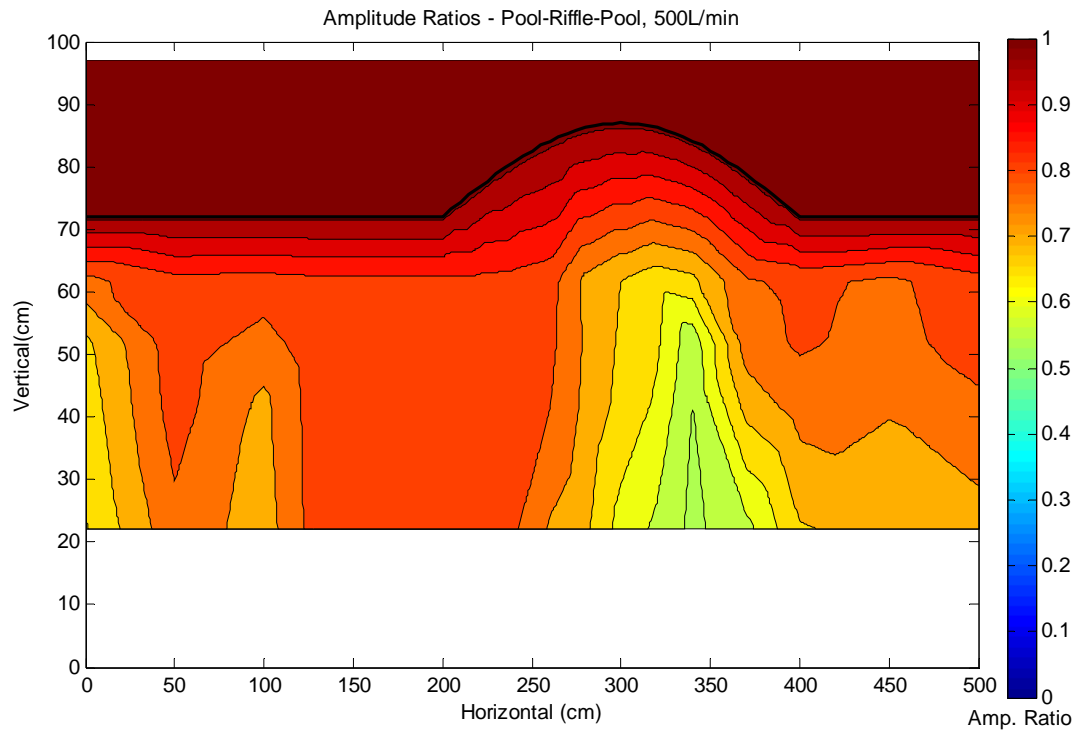


Figure 3.1.10. Temperature Amplitude Ratios, Trial 10: Pool-Riffle-Pool Topography, 500L/min Flow Rate, 6.4mm Grain Size

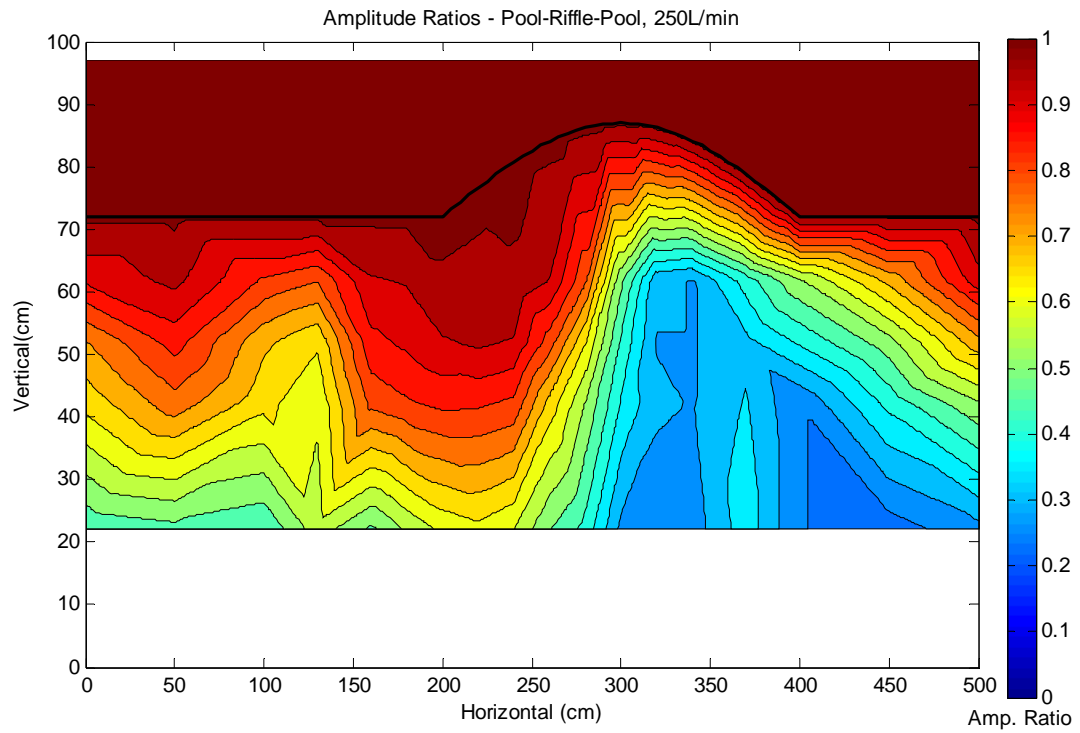


Figure 3.1.11. Temperature Amplitude Ratios, Trial 11: Pool-Riffle-Pool Topography, 250L/min Flow Rate, 6.4mm Grain Size

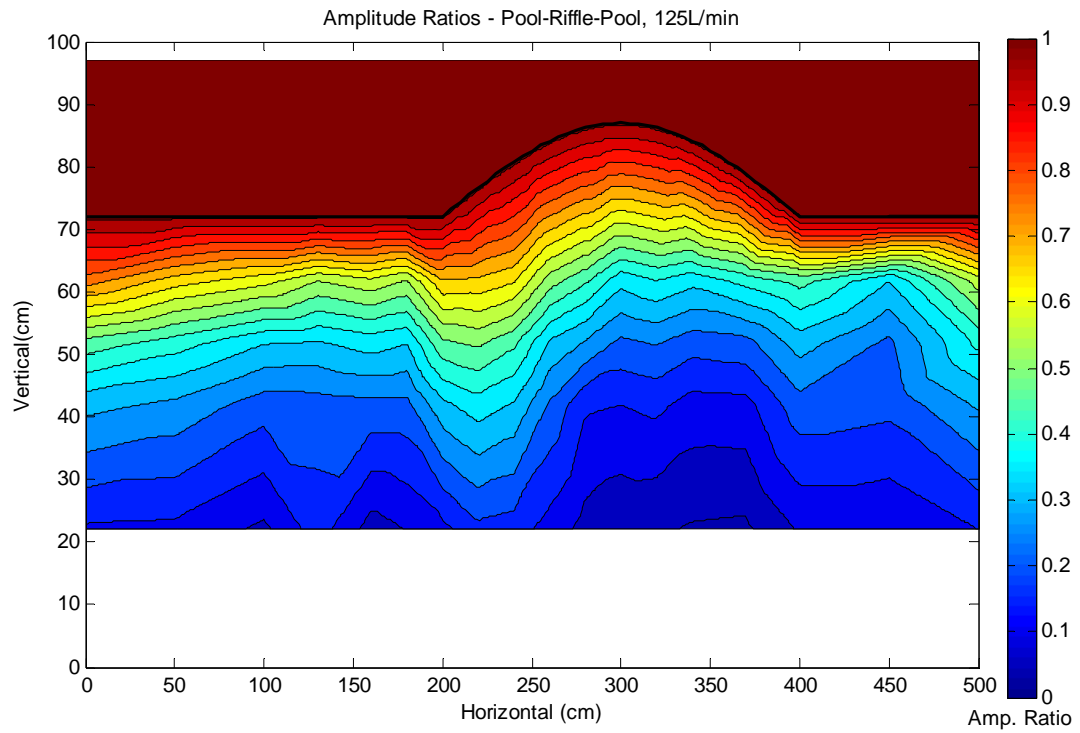


Figure 3.1.12. Temperature Amplitude Ratios, Trial 12: Pool-Riffle-Pool Topography, 125L/min Flow Rate, 6.4mm Grain Size

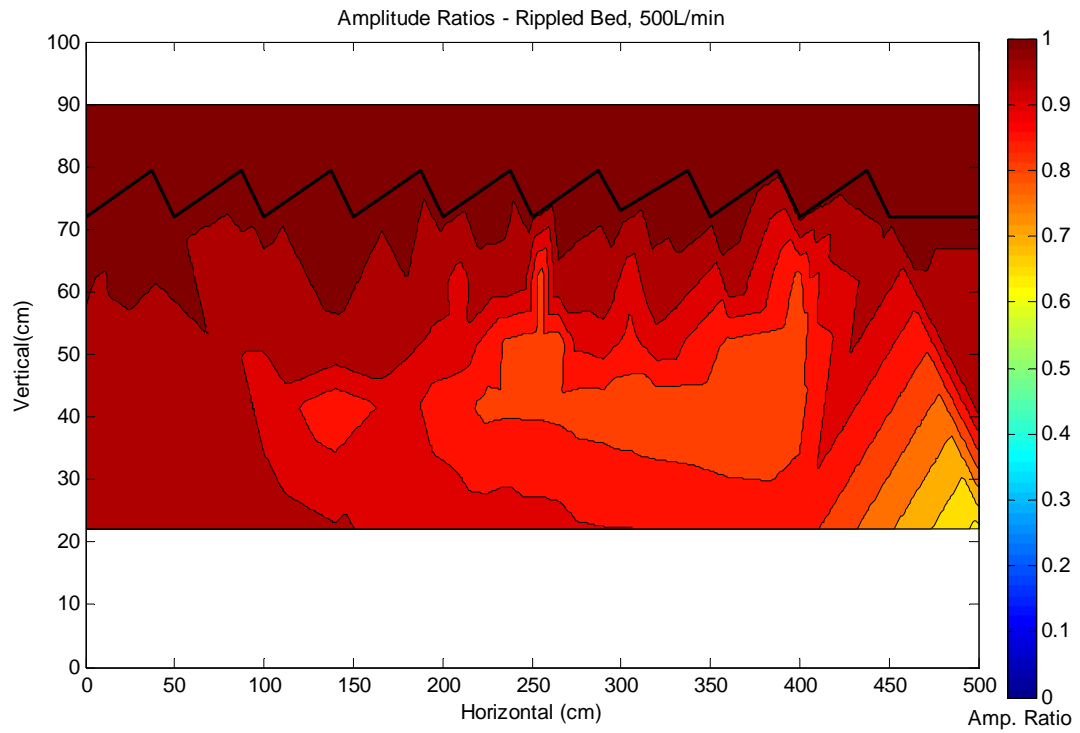


Figure 3.1.13. Temperature Amplitude Ratios, Trial 13: Rippled Bed Topography, 500L/min Flow Rate, 6.4mm Grain Size

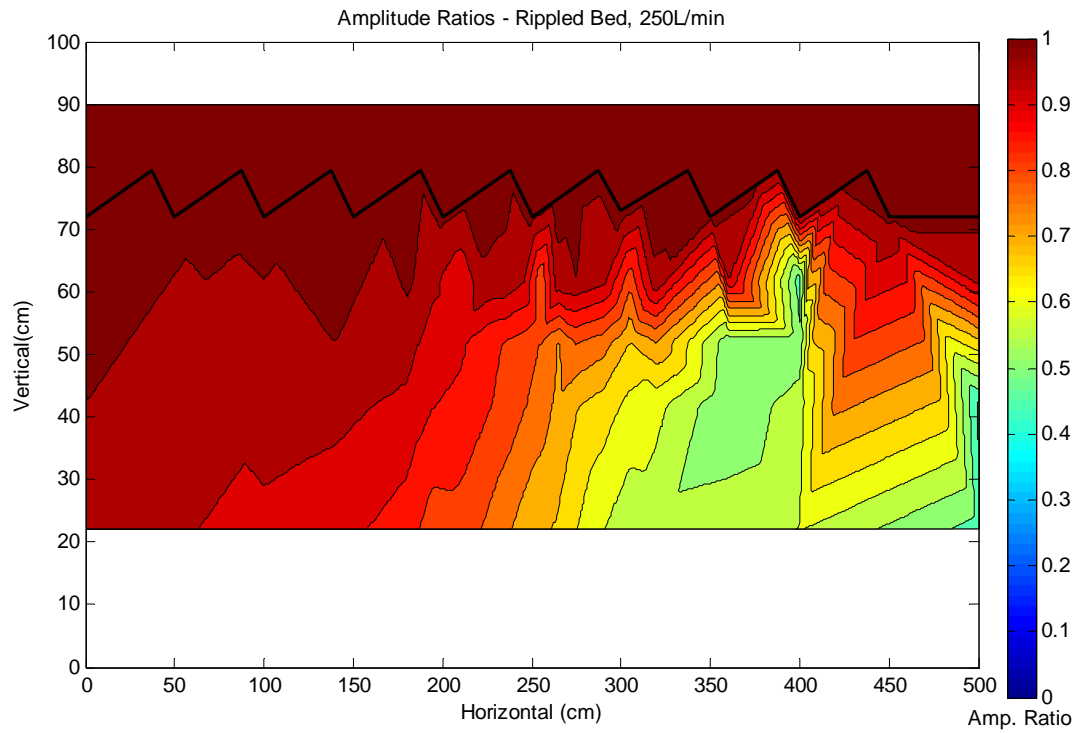


Figure 3.1.14. Temperature Amplitude Ratios, Trial 14: Rippled Bed Topography, 250L/min Flow Rate, 6.4mm Grain Size

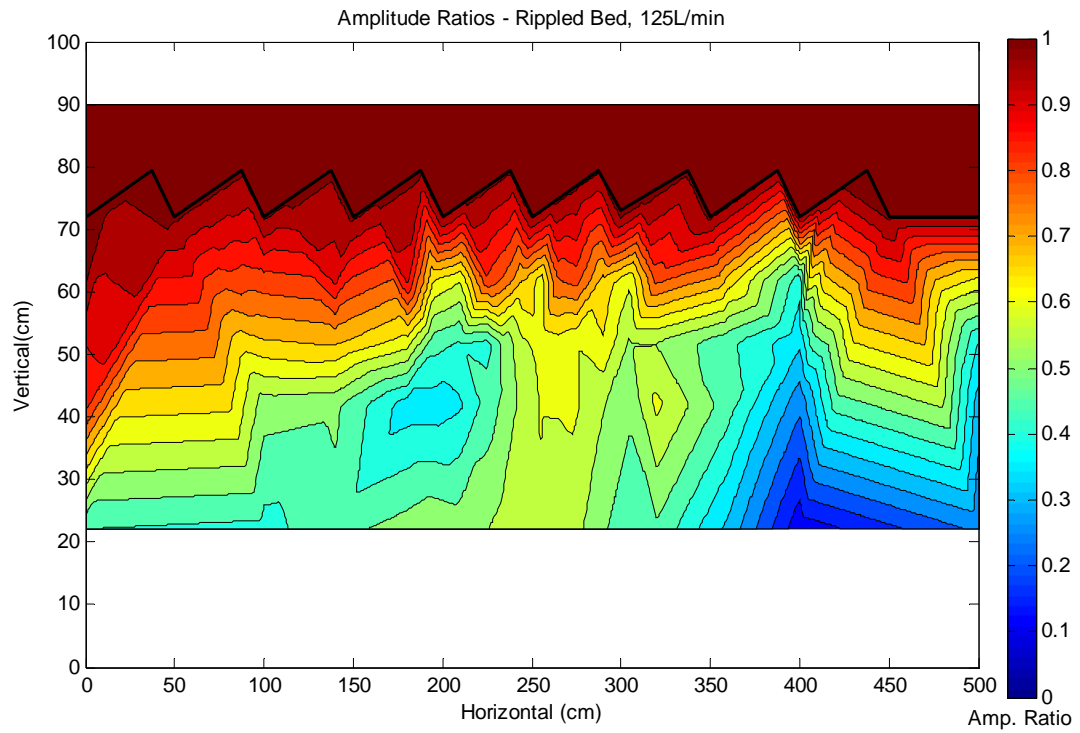


Figure 3.1.15. Temperature Amplitude Ratios, Trial 15: Rippled Bed Topography, 125L/min Flow Rate, 6.4mm Grain Size

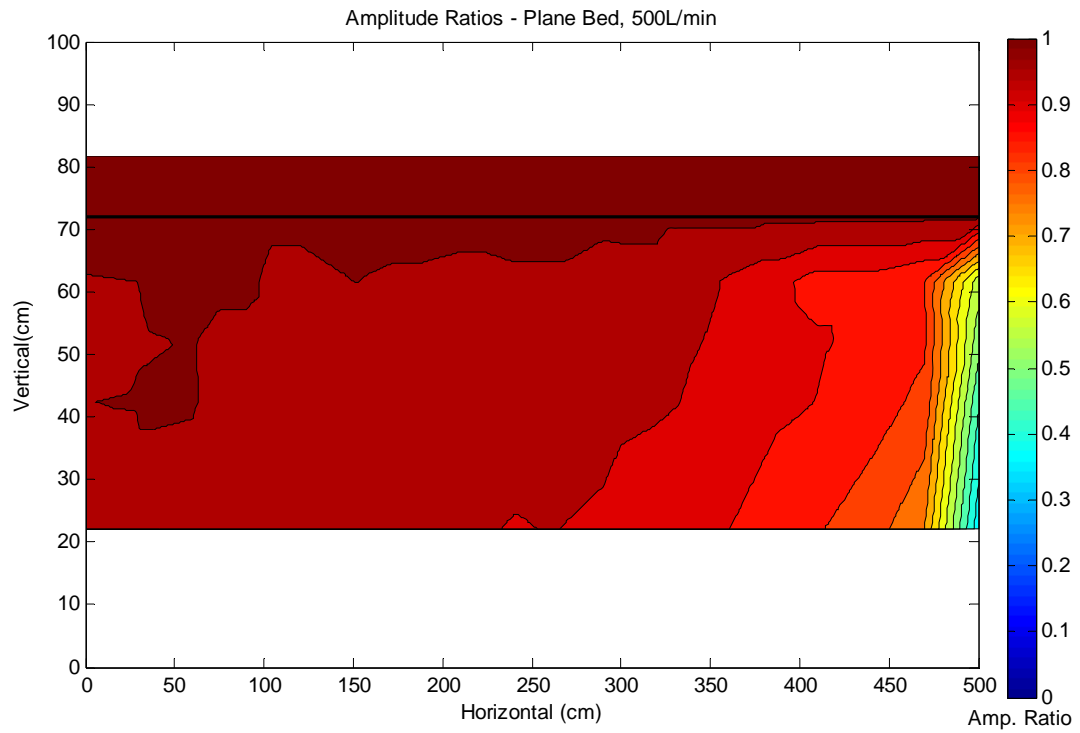


Figure 3.1.16. Temperature Amplitude Ratios, Trial 16: Plane Bed Topography, 500L/min Flow Rate, 6.4mm Grain Size

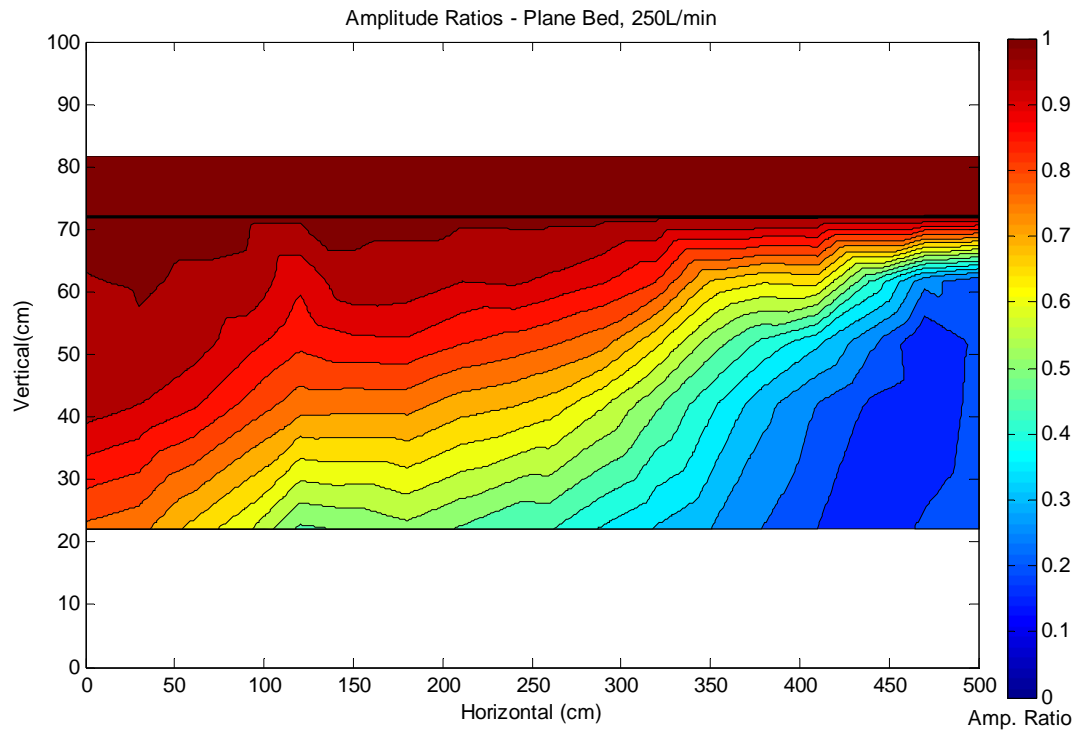


Figure 3.1.17. Temperature Amplitude Ratios, Trial 17: Plane Bed Topography, 250L/min Flow Rate, 6.4mm Grain Size

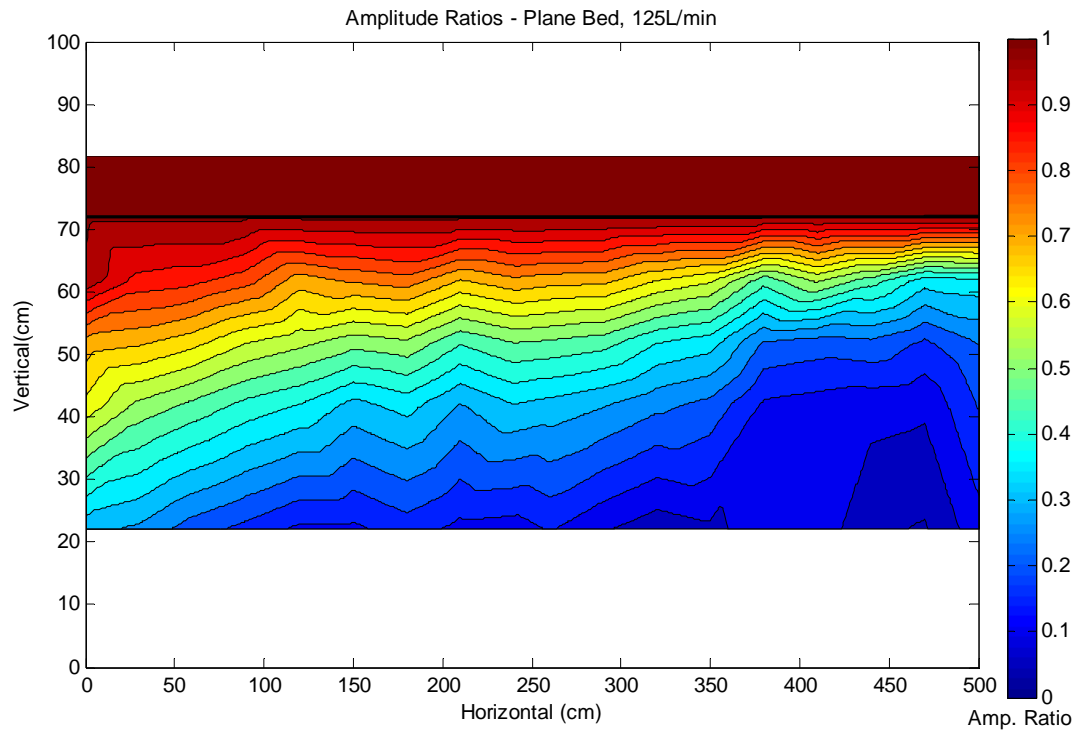


Figure 3.1.18. Temperature Amplitude Ratios, Trial 18: Plane Bed Topography, 125L/min Flow Rate, 6.4mm Grain Size

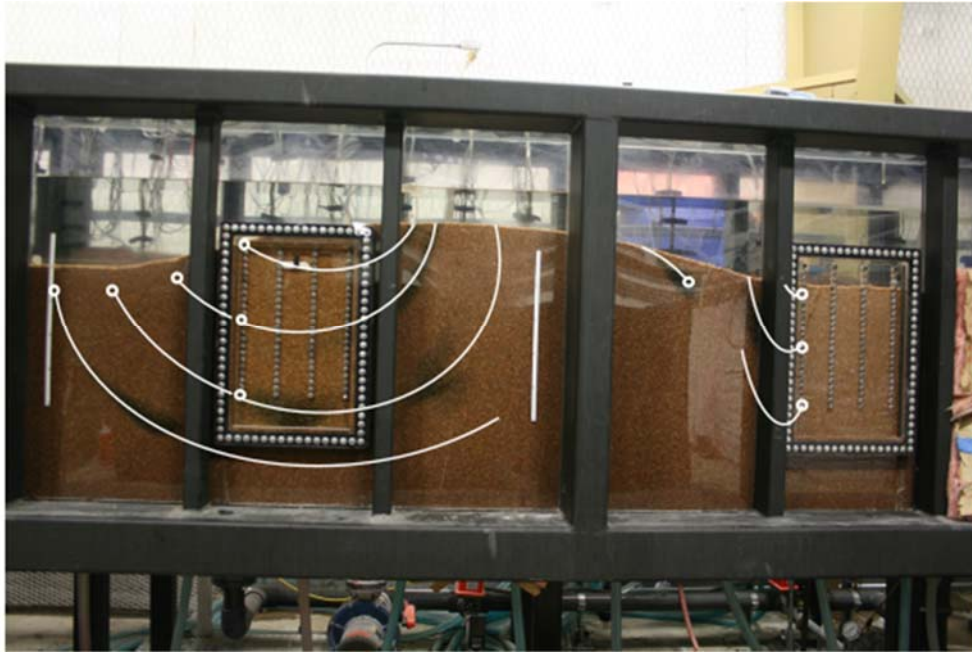


Figure 3.3.1. Dye Tracing Patterns, Trial 1: Pool-Riffle-Pool Topography, 500L/min Flow Rate, 2.4mm Grain Size. White circles indicate dye injection points. White lines indicate observed movement of dye, beginning at injection points and continuing until reaching the bed, or dispersing to the point where the dye can no longer be tracked with precision.

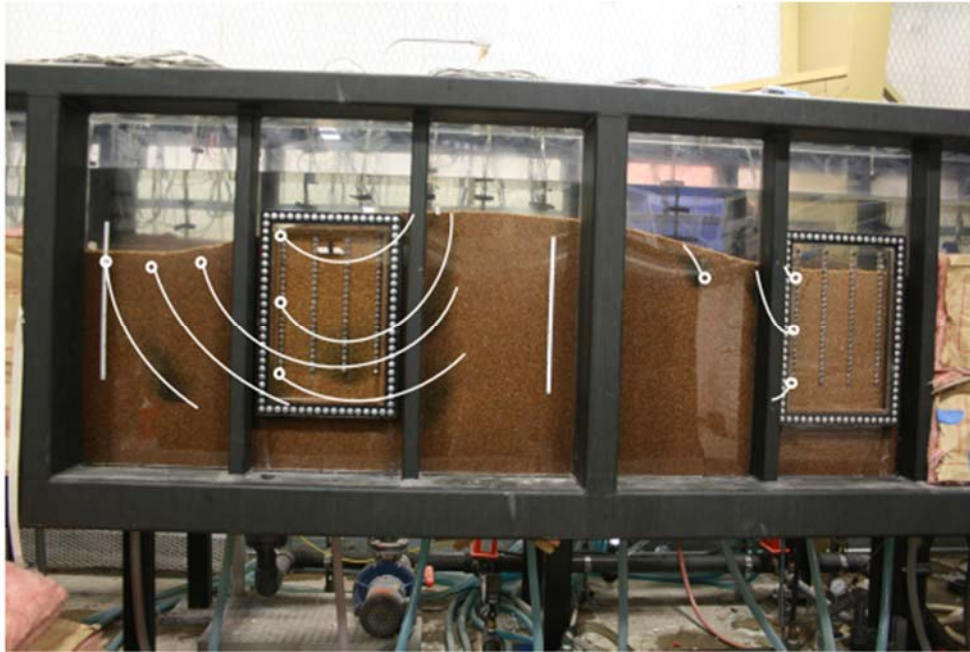


Figure 3.3.2. Dye Tracing Patterns, Trial 2: Pool-Riffle-Pool Topography, 250L/min Flow Rate, 2.4mm Grain Size. White circles indicate dye injection points. White lines indicate observed movement of dye, beginning at injection points and continuing until reaching the bed, or dispersing to the point where the dye can no longer be tracked with precision.



Figure 3.3.3. Dye Tracing Patterns, Trial 3: Pool-Riffle-Pool Topography, 125L/min Flow Rate, 2.4mm Grain Size. White circles indicate dye injection points. White lines indicate observed movement of dye, beginning at injection points and continuing until reaching the bed, or dispersing to the point where the dye can no longer be tracked with precision. Flow paths are not shown as most movement was directly downward in the first few minutes of the test, indicative of density driven advection, rather than bedform induced advection.

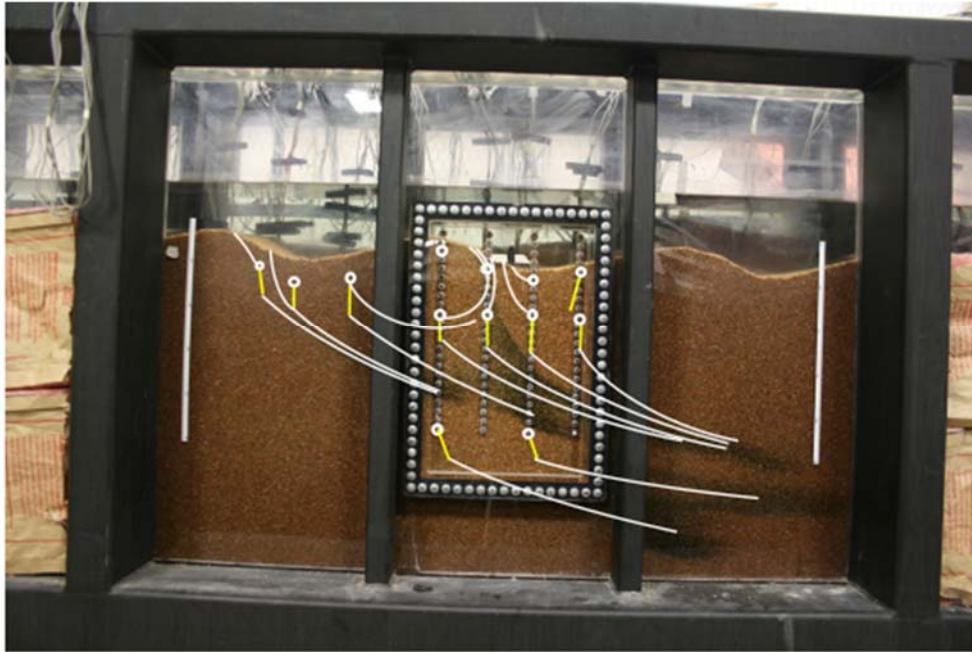


Figure 3.3.4. Dye Tracing Patterns, Trial 4: Rippled Bed Topography, 500L/min Flow Rate, 2.4mm Grain Size. White circles indicate dye injection points. White lines indicate observed movement of dye, beginning at injection points and continuing until reaching the bed, or dispersing to the point where the dye can no longer be tracked with precision. Yellow lines indicate rapid downward motion in the first few minutes of the trial, attributed to density driven advection rather than bedform driven advection.

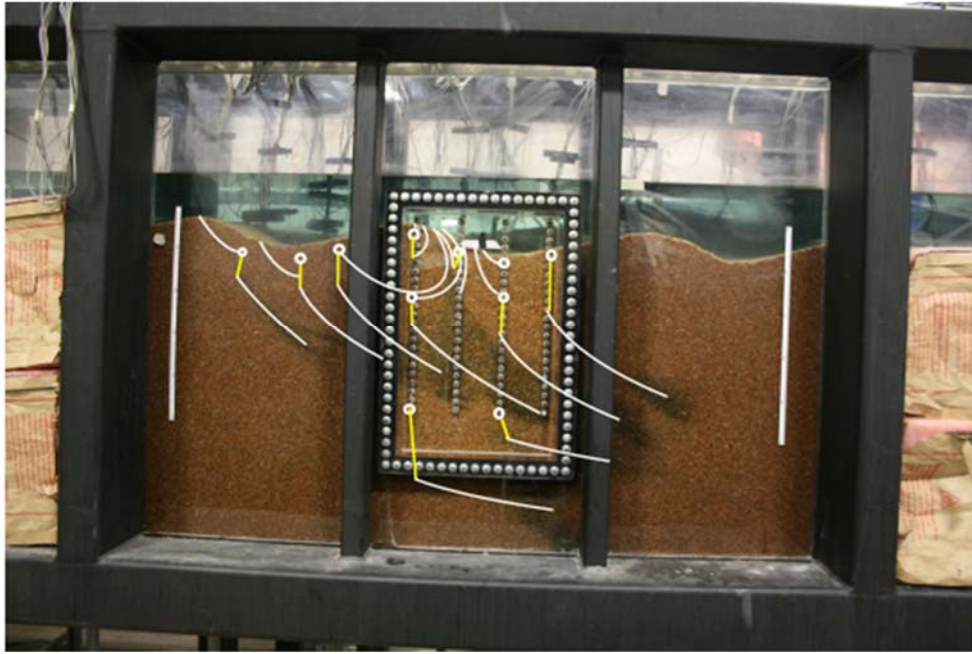


Figure 3.3.5. Dye Tracing Patterns, Trial 5: Rippled Bed Topography, 250L/min Flow Rate, 2.4mm Grain Size. White circles indicate dye injection points. White lines indicate observed movement of dye, beginning at injection points and continuing until reaching the bed, or dispersing to the point where the dye can no longer be tracked with precision. Yellow lines indicate rapid downward motion in the first few minutes of the trial, attributed to density driven advection rather than bedform driven advection.



Figure 3.3.6. Dye Tracing Patterns, Trial 6: Rippled Bed Topography, 125L/min Flow Rate, 2.4mm Grain Size. White circles indicate dye injection points. Flow paths are not shown as most movement was directly downward in the first few minutes of the test, indicative of density driven advection, rather than bedform induced advection.

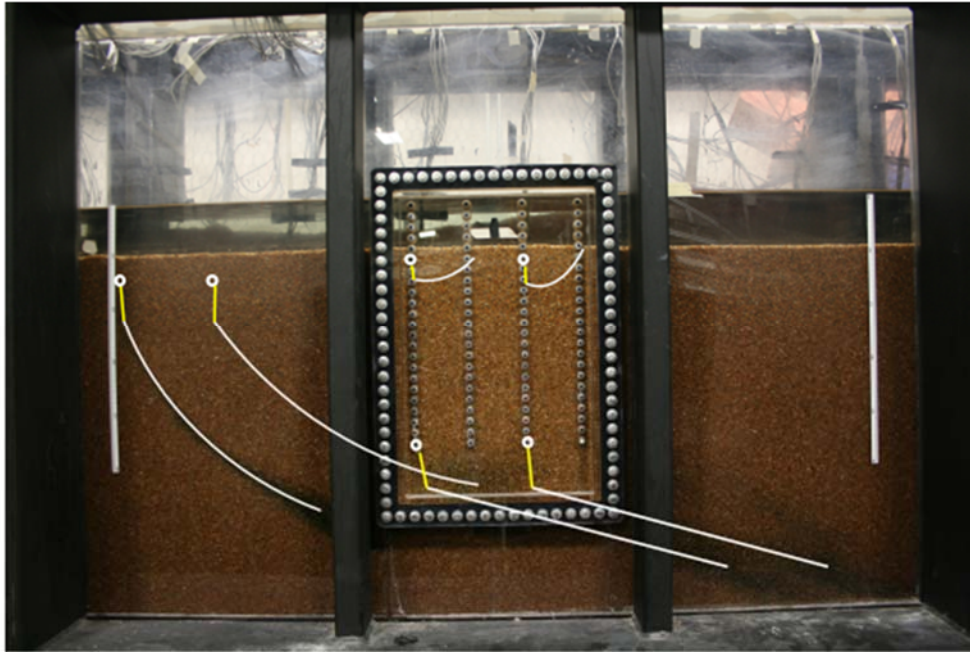


Figure 3.3.7. Dye Tracing Patterns, Trial 7: Plane Bed Topography, 500L/min Flow Rate, 2.4mm Grain Size. White circles indicate dye injection points. White lines indicate observed movement of dye, beginning at injection points and continuing until reaching the bed, or dispersing to the point where the dye can no longer be tracked with precision. Yellow lines indicate rapid downward motion in the first few minutes of the trial, attributed to density driven advection rather than bedform driven advection.

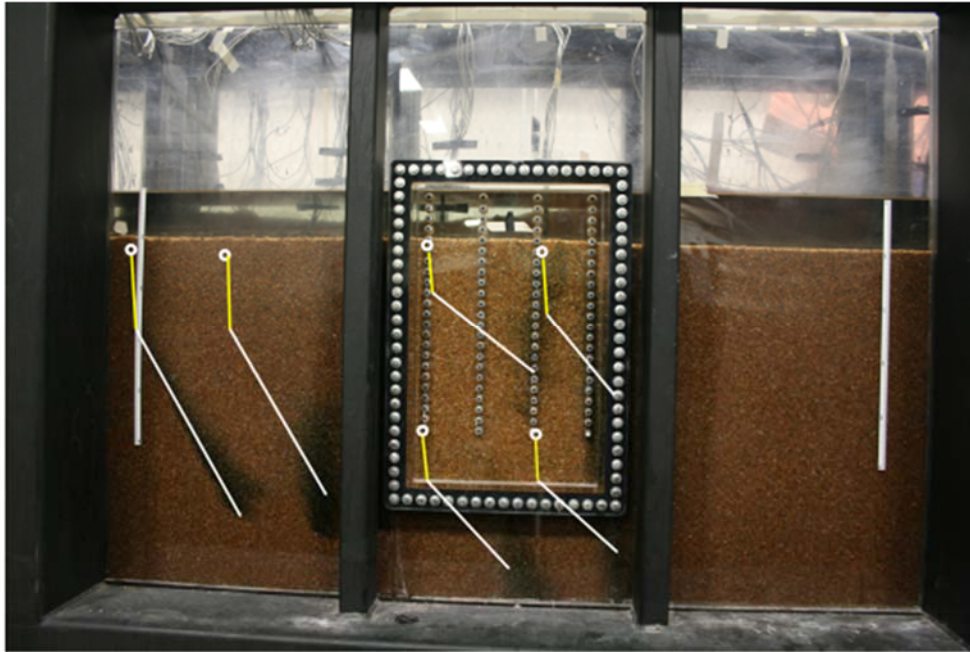


Figure 3.3.8. Dye Tracing Patterns, Trial 8: Plane Bed Topography, 250L/min Flow Rate, 2.4mm Grain Size. White circles indicate dye injection points. White lines indicate observed movement of dye, beginning at injection points and continuing until reaching the bed, or dispersing to the point where the dye can no longer be tracked with precision. Yellow lines indicate rapid downward motion in the first few minutes of the trial, attributed to density driven advection rather than bedform driven advection.

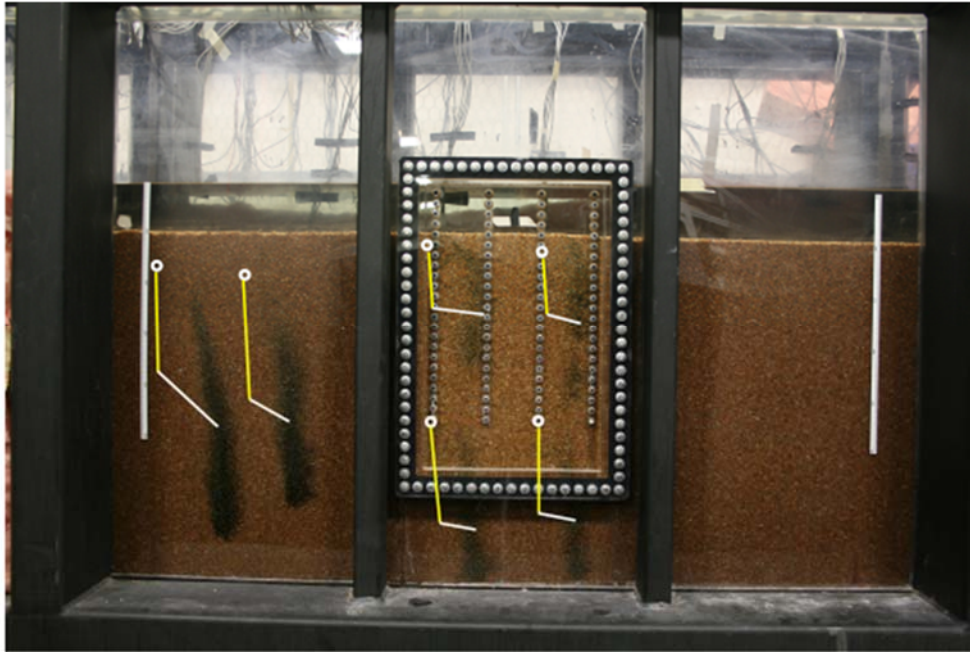


Figure 3.3.9. Dye Tracing Patterns, Trial 9: Plane Bed Topography, 125L/min Flow Rate, 2.4mm Grain Size. White circles indicate dye injection points. White lines indicate observed movement of dye, beginning at injection points and continuing until reaching the bed, or dispersing to the point where the dye can no longer be tracked with precision. Yellow lines indicate rapid downward motion in the first few minutes of the trial, attributed to density driven advection rather than bedform driven advection.

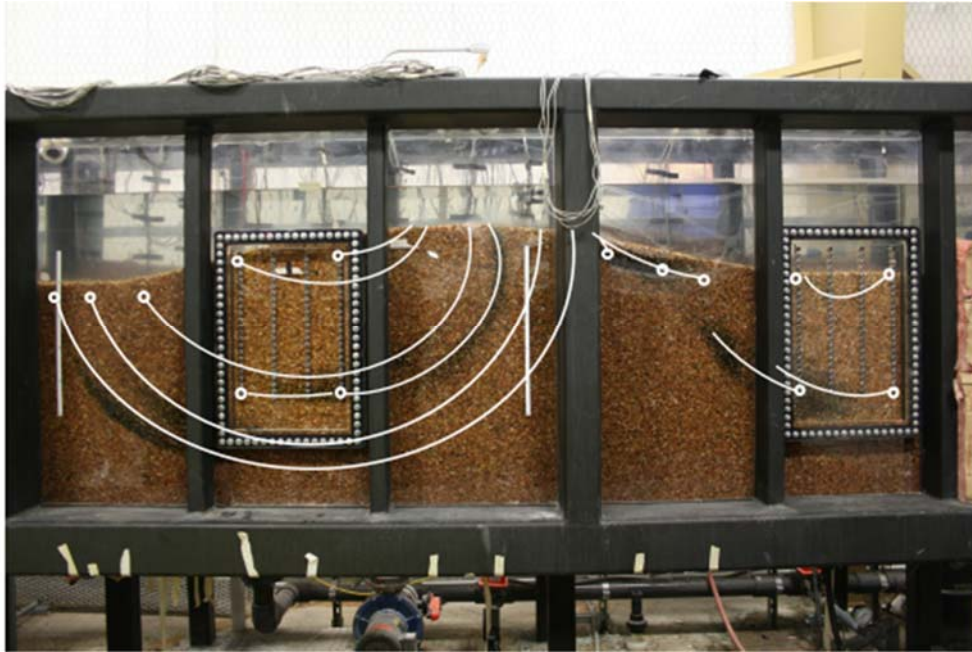


Figure 3.3.10. Dye Tracing Patterns, Trial 10: Pool-Riffle-Pool Topography, 500L/min Flow Rate, 6.4mm Grain Size. White circles indicate dye injection points. White lines indicate observed movement of dye, beginning at injection points and continuing until reaching the bed, or dispersing to the point where the dye can no longer be tracked with precision.

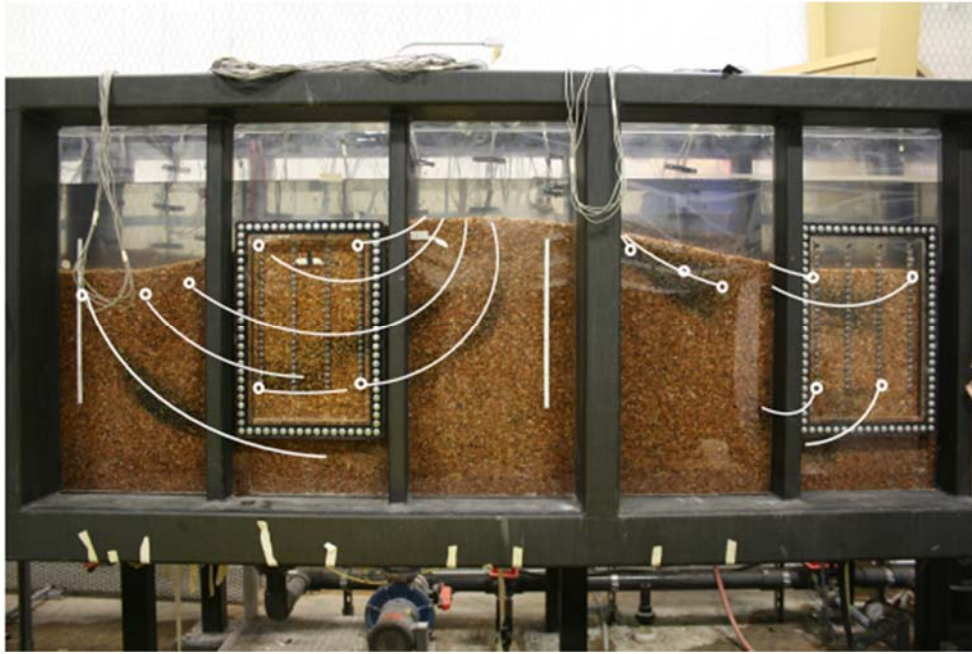


Figure 3.3.11. Dye Tracing Patterns, Trial 11: Pool-Riffle-Pool Topography, 250L/min Flow Rate, 6.4mm Grain Size. White circles indicate dye injection points. White lines indicate observed movement of dye, beginning at injection points and continuing until reaching the bed, or dispersing to the point where the dye can no longer be tracked with precision.

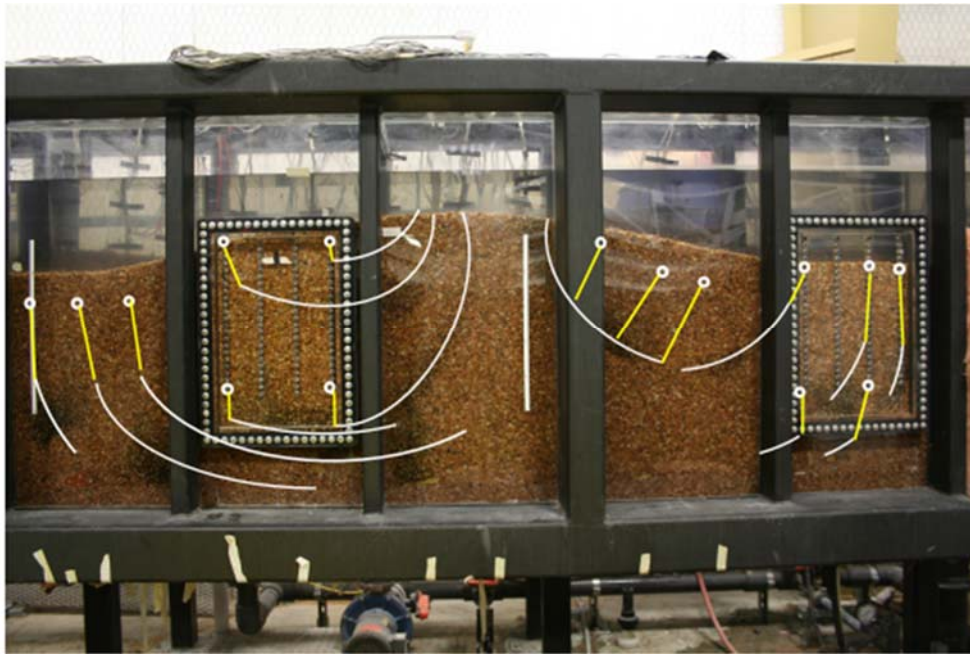


Figure 3.3.12. Dye Tracing Patterns, Trial 12: Pool-Riffle-Pool Topography, 125L/min Flow Rate, 6.4mm Grain Size. White circles indicate dye injection points. White lines indicate observed movement of dye, beginning at injection points and continuing until reaching the bed, or dispersing to the point where the dye can no longer be tracked with precision. Yellow lines indicate rapid downward motion in the first few minutes of the trial, attributed to density driven advection rather than bedform driven advection.



Figure 3.3.13. Dye Tracing Patterns, Trial 13: Rippled Bed Topography, 500L/min Flow Rate, 6.4mm Grain Size. White circles indicate dye injection points. White lines indicate observed movement of dye, beginning at injection points and continuing until reaching the bed, or dispersing to the point where the dye can no longer be tracked with precision.



Figure 3.3.14. Dye Tracing Patterns, Trial 14: Rippled Bed Topography, 250L/min Flow Rate, 6.4mm Grain Size. White circles indicate dye injection points. White lines indicate observed movement of dye, beginning at injection points and continuing until reaching the bed, or dispersing to the point where the dye can no longer be tracked with precision.

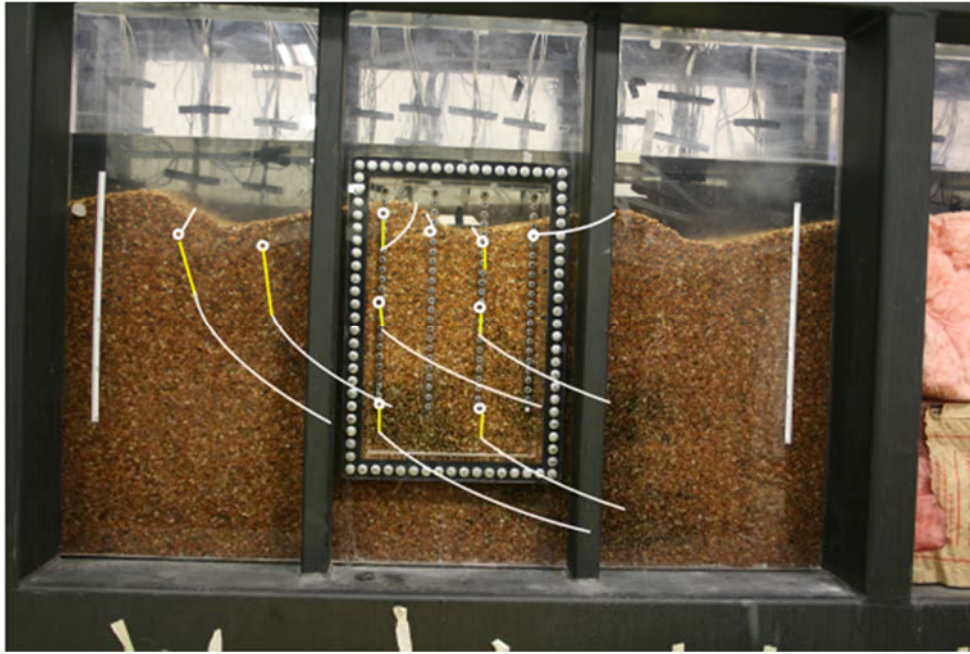


Figure 3.3.15. Dye Tracing Patterns, Trial 15: Rippled Bed Topography, 125L/min Flow Rate, 6.4mm Grain Size. White circles indicate dye injection points. White lines indicate observed movement of dye, beginning at injection points and continuing until reaching the bed, or dispersing to the point where the dye can no longer be tracked with precision. Yellow lines indicate rapid downward motion in the first few minutes of the trial, attributed to density driven advection rather than bedform driven advection.

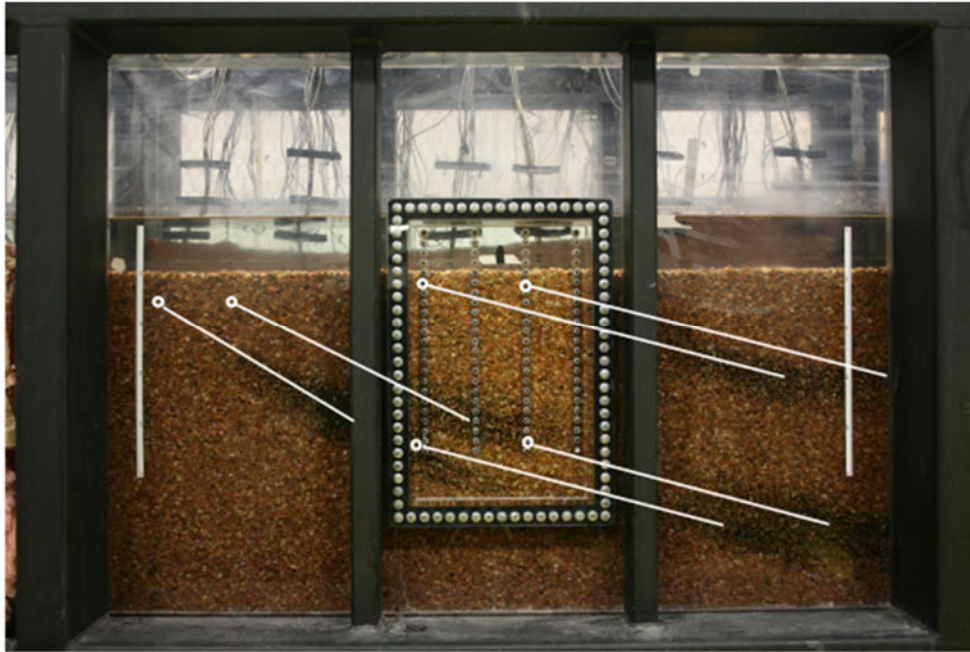


Figure 3.3.16. Dye Tracing Patterns, Trial 16: Plane Bed Topography, 500L/min Flow Rate, 6.4mm Grain Size. White circles indicate dye injection points. White lines indicate observed movement of dye, beginning at injection points and continuing until reaching the bed, or dispersing to the point where the dye can no longer be tracked with precision.



Figure 3.3.17. Dye Tracing Patterns, Trial 17: Plane Bed Topography, 250L/min Flow Rate, 6.4mm Grain Size. White circles indicate dye injection points. White lines indicate observed movement of dye, beginning at injection points and continuing until reaching the bed, or dispersing to the point where the dye can no longer be tracked with precision. Yellow lines indicate rapid downward motion in the first few minutes of the trial, attributed to density driven advection rather than bedform driven advection.



Figure 3.3.18. Dye Tracing Patterns, Trial 18: Plane Bed Topography, 125L/min Flow Rate, 6.4mm Grain Size. White circles indicate dye injection points. White lines indicate observed movement of dye, beginning at injection points and continuing until reaching the bed, or dispersing to the point where the dye can no longer be tracked with precision. Yellow lines indicate rapid downward motion in the first few minutes of the trial, attributed to density driven advection rather than bedform driven advection.

References

1. Alley, W. M., Healy, R. W., LaBaugh, J. W. & Reilly, T. E. Hydrology - Flow and storage in groundwater systems. *Science* **296**, 1985–1990 (2002).
2. Arrigoni, A. S. *et al.* Buffered, lagged, or cooled? Disentangling hyporheic influences on temperature cycles in stream channels. *Water Resour. Res.* **44**, (2008).
3. Bardini, L., Boano, F., Cardenas, M. B., Revelli, R. & Ridolfi, L. Nutrient cycling in bedform induced hyporheic zones. *Geochimica Et Cosmochimica Acta* **84**, 47–61
4. Battin, T. J., Kaplan, L. A., Newbold, J. D. & Hendricks, S. P. A mixing model analysis of stream solute dynamics and the contribution of a hyporheic zone to ecosystem function. *Freshw. Biol.* **48**, 995–1014 (2003).
5. Bouletreau, S., Salvo, E., Lyautey, E., Mastrotillo, S. & Garabetian, F. Temperature dependence of denitrification in phototrophic river biofilms. *Sci. Total Environ.* **416**, 323–328 (2012).
6. Boulton, A. J., Findlay, S., Marmonier, P., Stanley, E. H. & Valett, H. M. The functional significance of the hyporheic zone in streams and rivers. *Annu. Rev. Ecol. Syst.* **29**, 59–81 (1998).
7. Bourg, A. C. M. & Bertin, C. Diurnal variations in the water chemistry of a river contaminated by heavy metals: Natural biological cycling and anthropic influence. *Water Air Soil Pollut.* **86**, 101–116 (1996).
8. Bourg, A. C. M., Kedziorek, M. A. M. & Crouzet, C. Seasonal cycles of dissolved Cd, Mn and Zn in river water caused by variations in pH induced by biological

- activity. *Aquat. Geochem.* **6**, 461–471 (2000).
9. Brick, C. M. & Moore, J. N. Diel variation of trace metals in the upper Clark Fork River, Montana. *Environ. Sci. Technol.* **30**, 1953–1960 (1996).
 10. Brunke, M. & Gonser, T. The ecological significance of exchange processes between rivers and groundwater. *Freshw. Biol.* **37**, 1–33 (1997).
 11. Cardenas, M. B. & Wilson, J. L. Dunes, turbulent eddies, and interfacial exchange with permeable sediments. *Water Resour. Res.* **43**, (AUG 11 2007a).
 12. Cardenas, M. B. & Wilson, J. L. Effects of current-bed form induced fluid flow on the thermal regime of sediments. *Water Resour. Res.* **43**, (AUG 30 2007b).
 13. Cardenas, M. B. & Wilson, J. L. Thermal regime of dune-covered sediments under gaining and losing water bodies. *J. Geophys. Res.-Biogeosci.* **112**, (DEC 21 2007c).
 14. Church, M. in *Annual Review of Earth and Planetary Sciences* **34**, 325–354 (Annual Reviews, 2006).
 15. Davy-Bowker, J., Sweeting, W., Wright, N., Clarke, R. T. & Arnott, S. The distribution of benthic and hyporheic macroinvertebrates from the heads and tails of riffles. *Hydrobiologia* **563**, 109–123 (2006).
 16. Einsele, G. *Sedimentary Basins; Evolution, Facies, and Sediment Budget*. (Springer, 2000).
 17. Findlay, S. Importance of Surface-Subsurface Exchange in Stream Ecosystems - the Hyporheic Zone. *Limnol. Oceanogr.* **40**, 159–164 (1995).
 18. Franken, R. J. M., Storey, R. G. & Williams, D. D. Biological, chemical and physical

- characteristics of downwelling and upwelling zones in the hyporheic zone of a north-temperate stream. *Hydrobiologia* **444**, 183–195 (2001).
19. Janssen, F. *et al.* A comparative experimental and multiphysics computational fluid dynamics study of coupled surface-subsurface flow in bed forms. *Water Resour. Res.* **48**, (2012).
 20. Jones, C. A., Nimick, D. A. & McCleskey, R. B. Relative effect of temperature and pH on diel cycling of dissolved trace elements in Prickly Pear Creek, Montana. *Water Air Soil Pollut.* **153**, 95–113 (2004).
 21. Mermillod-Blondin, F., Des Chatelliers, M. C., Marmonier, P. & Dole-Olivier, M. J. Distribution of solutes, microbes and invertebrates in river sediments along a riffle-pool-riffle sequence. *Freshw. Biol.* **44**, 255–269 (2000).
 22. Morris, J. M. & Meyer, J. S. Photosynthetically mediated Zn removal from the water column in High Ore Creek, Montana. *Water Air Soil Pollut.* **179**, 391–395 (2007).
 23. Mutz, M., Kalbus, E. & Meinecke, S. Effect of instream wood on vertical water flux in low-energy sand bed flume experiments. *Water Resour. Res.* **43**, (2007).
 24. Nimick, D. A., Cleasby, T. E. & McCleskey, R. B. Seasonality of diel cycles of dissolved trace-metal concentrations in a Rocky Mountain stream. *Geochim. Cosmochim. Acta* **69**, A770–A770 (2005).
 25. Nimick, D. A. *et al.* Diel cycles in dissolved metal concentrations in streams: Occurrence and possible causes. *Water Resour. Res.* **39**, (2003).
 26. Rudall, S. & Jarvis, A. P. Diurnal fluctuation of zinc concentration in metal polluted

- ivers and its potential impact on water quality and flux estimates. *Water Science and Technology* **65**, 164–170 (2012).
27. Sawyer, A. H., Cardenas, M. B. & Buttlers, J. Hyporheic temperature dynamics and heat exchange near channel-spanning logs. *Water Resour. Res.* **48**, (2012).
 28. Simons, D. B. & Richardson, E. V. *Resistance to Flow in Alluvial Channels*. (U.S. Government Printing Office, 1966).
 29. Simons, D. B. & Senturk, F. *Sediment Transport Technology: Water and Sediment Dynamics*. (Water Resources Publications, 1992).
 30. Stanford, J. A. & Ward, J. V. The Hyporheic Habitat of River Ecosystems. *Nature* **335**, 64–66 (1988).
 31. Stanford, J. A. *et al.* A general protocol for restoration of regulated rivers. *Regulated Rivers - Research and Management* **12**, 391–413 (1996).
 32. Storey, R. G. & Williams, D. D. Spatial responses of hyporheic invertebrates to seasonal changes in environmental parameters. *Freshw. Biol.* **49**, 1468–1486 (2004).
 33. Storey, R. G., Williams, D. D. & Fulthorpe, R. R. Nitrogen processing in the hyporheic zone of a pastoral stream. *Biogeochemistry* **69**, 285–313 (2004).
 34. Swanson, T. E. & Cardenas, M. B. Diel heat transport within the hyporheic zone of a pool-riffle-pool sequence of a losing stream and evaluation of models for fluid flux estimation using heat. *Limnol. Oceanogr.* **55**, 1741–1754 (2010).
 35. Trimmer, M. *et al.* River bed carbon and nitrogen cycling: State of play and some new directions. *Sci. Total Environ.* **434**, 143–158 (2012).

36. Veraart, A. J., de Klein, J. J. M. & Scheffer, M. Warming can boost denitrification disproportionately due to altered oxygen dynamics. *PloS one* **6**, (2011).
37. Vervier, P., Bonvallet-Garay, S., Sauvage, S., Valett, H. M. & Sanchez-Perez, J.-M. Influence of the hyporheic zone on the phosphorus dynamics of a large gravel-bed river, Garonne River, France. *Hydrol. Process.* **23**, 1801–1812 (2009).
38. Wondzell, S. M. The role of the hyporheic zone across stream networks. *Hydrol. Process.* **25**, 3525–3532 (2011).
39. Zarnetske, J. P., Haggerty, R., Wondzell, S. M. & Baker, M. A. Dynamics of nitrate production and removal as a function of residence time in the hyporheic zone. *J. Geophys. Res.-Biogeosci.* **116**, (2011).
40. Zlotnik, V. A., Cardenas, M. B. & Toundykov, D. Effects of Multiscale Anisotropy on Basin and Hyporheic Groundwater Flow. *Ground Water* **49**, 576–583 (2011).